Boosting Hot Electrons in Hetero-Superstructures for Plasmon-Enhanced Catalysis

Jun Guo,[†,‡,§,‡] Yin Zhang,[†,‡,§,‡] Lin Shi,[†] Yanfei Zhu,[†,§] Megersa F. Mideksa,[†] Ke Hou,[†,‡,§] Wenshi Zhao,[†,§] Dawei Wang,[†] Meiting Zhao,[#] Xiaofei Zhang,[†] Jiawei Lv,[†] Jianqi Zhang,[†] Xiaoli Wang*[,†] and Zhiyong Tang*[,†]

[†]CAS Key Laboratory of Nanosystem and Hierarchical Fabrication, CAS Center for Excellence in Nanoscience, National Center for Nanoscience and Technology, Beijing 100190, P. R. China

[‡]Center for Nanochemistry, Peking University, Beijing 100871, P. R. China

[§]University of Chinese Academy of Sciences, Beijing 100049, P. R. China

[#]School of Materials Science and Engineering, Nanyang Technological University, Singapore 639798, Singapore

KEYWORDS: Hetero-structures; plasmon; superstructures; hot electrons; photocalysis

ABSTRACT: Hetero-nanostructures featured with both strong plasmon absorption and high catalytic activity are believed to be ideal platforms to realize efficient light-driven catalysis. However, in reality it remains great challenge to acquire high performance catalysis in such hetero-nanostructures due to poor generation and transfer of plamson-induced hot electrons. In this report, we demonstrate that Au nanorod@Pd superstructures (Au@Pd SSs), where the ordered Pd nanoarrays are precisely grown on Au nanorod surfaces via solution-based seed-mediated approach, would be an excellent solution for this challenge. Both experiment and theory disclose that the ordered arrangement of Pd on Au nanorod surfaces largely promotes hot electron generation and transfer via amplified local electromagnetic field and decreased electron-phonon coupling, respectively. Each effect is separately highlighted in experiment by the significant plasmon-enhanced catalytic activity of Au@Pd SSs in two types of important reactions with distinct timescale of bond-dissociation event: molecular oxygen activation and carbon-carbon coupling reaction. This work opens the door to design and application of new generation photocatalysts.

Introduction

Plasmonic nanostructures have been one of the hottest research topics in photocatalysis[1] by virtue of their highly focused electromagnetic field, effective photothermal conversion, and unique hot electron generation. Among those catalysis-favored characteristics, hot electrons produced from Landau damping of localized surface plasmon resonance (SPR) trigger extraordinary interest owing to their potentials to not only greatly promote chemical transformations via light-energy conversion[2] but also offer new pathway to manipulate product selectivity through specific transfer into substrate orbitals[3]. More intriguingly, integration of multiple compositions into the plasmonic hetero-nanostructures would offer the additional opportunity for many valuable but challenging catalytic reactions, for instance, reverse water-gas shift[3d] and epoxidation of olefin[4].

In spite of its potential, current advance of plasmon-enhanced catalysis towards real reactions is causing serious concerns mainly because of low utilization of hot electrons. Efficient conversion of light energy to hot electrons generation requires that noble metal nanoparticles (NPs) are of strong and broad SPR absorption in solar spectrum, and Au[5] or Ag[6] NPs thus become the best candidates. Unfortunately, the relatively inert catalytic activities of plasmonic Au and Ag NPs are detrimental for efficient hot electrons injection into reactants[7]; meanwhile the hot electrons generated in these NPs are prone to self-thermalization and eventually cooled by ultrafast electron-phonon scattering[8], which seriously hinders their transfer to the catalytically active sites. To alleviate undesired energy dissipation, a poplar strategy is attachment of semiconductors like CdSe[9] and TiO_2[10] onto plasmonic NPs, facilitating hot electron transfer and utilization. However, as-formed Schottky barrier between metal and semiconductor determines that only a small portion of high-energy hot electrons can be used in catalysis[11]. Alternatively, to hybridize Au or Ag NPs with other transition metals like Pd and Pt might avoid formation of the energy barrier as well as improve the catalytic activity of resultant hetero-nanostructures. But, without understanding of structural design principle, such hybridization[12] would severely shield the original

SPR absorption and screen the local electromagnetic filed, consequently causing low hot electron generation efficiency.

Herein, we propose that hetero-superstructures with ordered multi-components are of superior ability to promote the plasmon-involved catalysis via function synergy between different constituents and performance optimization from structure organization. In detail, a facile and easily scaled-up strategy is developed to directly grow ordered Pd nanoarrays on Au nanorod (NR) surfaces for formation of the first example of freestanding hetero-superstructures, namely, Au nanorod@Pd superstructures (Au@Pd SSs). Design and preparation of the Au@Pd SSs are encouraged by the following fact. Plasmonic Au NRs inside are able to engender abundant hot electrons with the help of strong antenna effect of ultra-sharp Pd nanoarrays, while the ordered arrangement of Pd nanoarrays on-rod not only exposures rich active sites for incoming reactants but also prolongs the lifetime of hot electrons for efficient transfer and injection. Therefore, the well-defined composition and structure inherent in Au@Pd SSs will enable them to become novel plasmon-enhanced catalysts of high efficiency.

Experimental Section

Synthesis of Au@Pd SSs. Firstly, Au NRs were synthesized according to literature[13] with slight modification and used as seeds solution (see methods in supporting information). Secondly, 200 μL of 10 mM Na_2PdCl_4 and 2 mL Au NRs of aspect ratio (AR) being equal to 2.0 seeds solution were successively added into 20 mL of 10 mM hexadecylpyridinium chloride monohydrate (CPC) solution at 65°C. In subsequence, 400 μL of 100 mM freshly prepared ascorbic acid (AA) solution was injected. After 2 min vigorously stirring, the obtained solution was incubated for 30 min. Final products were collected by centrifugation at 8000 rpm for 5 min and re-dispersed in water for further use.

Synthesis of Au@Pd Nanodendrites (Au@Pd NDs). Briefly, 80 μL of 10 mM Na_2PdCl_4 and 2 mL of Au NR (AR = 2.5) seeds solution were successively added into 20 mL of 10 mM hexadecyltrimethylammonium chloride (CTAC) solution under 45°C. Subsequently, 400 μL of 100 mM freshly prepared AA solution was injected. After 2 min vigorously stirring, the growth solution was aged for 3 h. Final products were isolated by centrifugation at 8000 rpm for 5 min and re-dispersed in water for further use.

Synthesis of Au@Pd Core-shell Structures (Au@Pd CSs). Au@Pd CSs were synthesized by a method from literature[14]. In brief, 40 μL of 10 mM Na_2PdCl_4, 2 mL of Au NRs (AR = 2.8) seeds solution and 160 μL of 1.0 M HCl were successively added into 20 mL of 100 mM hexadecyltrimethylammonium bromide (CTAB) solution under 50°C. Subsequently, 100 μL of 100 mM freshly prepared AA solution was injected. After 2 min vigorously stirring, the growth solution was left undisturbed for 3 h. Final products were isolated by centrifugation at 8000 rpm for 5 min and re-dispersed in water for further use.

Transient Absorption and Pump-probe Measurements. Femtosecond transient absorption spectra were recorded by a pump-probe spectrometer (ExciPro, CDP) together with an amplified Ti:sapphire laser source (800 nm with a repetition rate of 1 kHz, Coherent). The 800 nm laser was split into two portions: the larger portion was passed through a BBO crystal to offer the pump light (pulse width < 35 fs; output energy ~7 μJ/pulse at the sample cell), and the other part was focused onto a sapphire plate to generate white light continuum. The obtained white light was split into two beams again, one as the probe light and the other as the reference light, in order to revise the pulse-to-pulse intensity fluctuations. Time delays between the pump and probe light were controlled by a motorized optical delay line. The spectral and temporal profiles of the transient absorbance changes were recorded by a 1024-pixel imaging spectrometer (CDP2022i) and the data at desired probe wavelength were plotted as a function of delay time by further processing at ExiPro 2.8.6 software. All samples (optical densities were similar at pump wavelength) were dispersed in water and subsequently sealed in a transparent cell during measurements, which was mounted on a rotating stage for keeping the pump-excited fraction of sample fresh. All measurements were undertaken under ambient condition.

Reactive Oxygen Species (ROS) Detection and Evaluation. For the evaluation of produced ROS, different nanostructures including Au@Pd SSs, Au@Pd NDs, Au@Pd CSs, bare Au NRs, porous Pd NPs, and the mixture of Au NRs and porous Pd NPs were tested under both dark environment and light irradiation (300 W Xe lamp with 510 nm long-pass filter, the effective power density of incident light was 0.7 W cm^{-2}) for systematic comparison. To exclude the thermal influence of irradiation, the incubation temperature was strictly controlled at 30°C with a circulating cooling system procedure. For the evaluation of singlet oxygen ($^1O_2$) specie, 10 μL of 1.0 M 2,2,6,6-tetramethyl-4-piperidine (TEMP) aqueous solution was injected into 100 μL of each nanostructures solution (final Au and Pd amounts of tested solution were listed in Tab. S1, according to ICP-MS results). The mixture was incubated under dark environment or light irradiation at 30°C for 20 min, and then characterized with electron spin resonance (ESR) spectroscopy at 20°C immediately. The amount of $^1O_2$ species was quantitatively calculated from the ESR signal intensity of TEMP-$^1O_2$ adduct by using the peak to peak height of the second line of spectrum method[15] and was normalized by dividing the Pd amount of each catalyst for parallel comparison.

Carbon-carbon Coupling Reaction. In a quartz reaction cell, benzeneboronic acid (24.4 mg, 0.2 mmol), NaOH (20.0 mg, 0.5 mmol), CTAB (36.0 mg, 0.1 mmol), iodobenzene (17 μL, 0.15 mmol) and the tested nanostructures (element amounts were listed in Tab. S1, according to ICP-MS results) were mixed with 2 mL of water/ethanol solvent (3:1 volume/volume) under stirring. The reaction was performed under dark environment or

light irradiation (300 W Xe lamp with 510 nm long-pass filter, the effective power density of incident light was 0.7 W cm^{-2}). To exclude the thermal influence under light irradiation, the incubation temperature was strictly controlled at 40°C with a circulating cooling system procedure. Products were characterized by gas chromatography–mass spectrometry (GC-MS, Thermo DSQ) with a TR-5MS column (30 m × 0.25 mm × 0.25 μm) and the turnover frequency (TOF) was calculated from the yield at 30 min based on total Pd amount.

Finite-difference Time-domain (FDTD) Simulation. The electric field distributions were calculated using Lumerical Solutions, a commercially available FDTD simulation software package. Simulations were performed in three-dimensional (3D) layout. A unit cell of 1000 nm × 1000 nm × 1200 nm along the x-axis, the y-axis and the z-axis, respectively, was set for each nanostructure and was calculated using perfectly matched layers (PML) in 3D as boundary condition. Total-field scattered-field (TFSF) waves at the range of 400-900 nm were injected to the unit cell along the + y direction, and a two-dimensional (2D) frequency-domain field profile monitor in x-z plane was used to collect field profile data. The mesh size was set to be 0.5 nm. The complex refractive indexes of Pd and Au were utilized from the data of Palik and Johnson & Christy, respectively. The background index of water was set to be 1.33. The shape and size of each Au@Pd nanostructure as well as Au NR were determined according to the average ones measured from corresponding TEM results.

Characterization. Visible Near-infrared (Vis-NIR) absorption spectrum were collected by Perkin Elmer Lambda 950 spectrophotometer. Transmission electron microscopy (TEM) images, high angle annular dark field scanning transmission electron microscopy (HAADF-STEM) imaging and energy-dispersive X-ray spectroscopy (EDX) elemental mapping were performed on Tecnai G2 F20 S-TWIN with an acceleration voltage of 200 kV. Small angle X-ray scattering (SAXS) profiles were recorded by a Rigaku NANO-Viewer (Cu Kα radiation) with a camera length of 700 mm operated at 40 kV and 30 mA. Wide-angle powder x-ray diffraction (XRD) patterns were obtained on D/MAX-TTRIII (CBO) with Cu Kα radiation (λ = 1.542 Å) operating at 40 kV and 200 mA. The inductively coupled plasma mass spectrometry (ICP-MS) data were taken from NexION 300X (Perkin Elmer). Dynamic light scattering (DLS) was characterized by Zetasizer Nano ZS. Electron spin resonance (ESR) spectra were recorded by Bruker (E500) ESR spectroscopy under following parameter settings: microwave power, 10.0 mW; frequency, 9.8 GHz; time constant, 40.0 ms; sweep width, 100.0 G.

Results and Discussion

Characterization of Au@Pd SSs. As-obtained products were firstly examined by transmission electron microscopy (TEM) and high resolution transmission electron microscope (HRTEM) imaging. As shown in Fig. 1a and Supplementary Fig. 1a, the Au@Pd SSs appear in monodisperse mace-like nanostructures, where inner Au NR cores are homogeneously surrounded by Pd nanoarray shells. HRTEM images (Fig. 1b and Fig. S1b,c) clearly indicate that Pd nanoarrays with average length of 6.9 nm (Fig. S8c) are perpendicularly arranged on the surfaces of Au NRs. Such Au@Pd core-shell nanostructures can be further verified by high-angle annular dark-field scanning transmission-electron microscopy (HAADF-STEM) and corresponding energy dispersive X-ray (EDX) elemental mapping images (Fig. 1c-e). The crystalline nature of the Au@Pd SSs is revealed by HRTEM and powder X-ray diffraction (PXRD) survey. In Fig. 1b, the clear fringe of 0.20 nm is ascribed to face-centered cubic (fcc) Au (200) plane, while another two sets of lattices with periodic spacing of 0.19 and 0.22 nm are assigned to fcc Pd (200) and Pd (111) lattice planes, respectively. Analogously, PXRD peaks (Fig. S2) of the Au@Pd SSs match well with combination of standard indexes of fcc Au (JCPDS no.04-0784) and fcc Pd (JCPDS no.46-1043), indicating that the products are highly crystalline without other impurity phase.

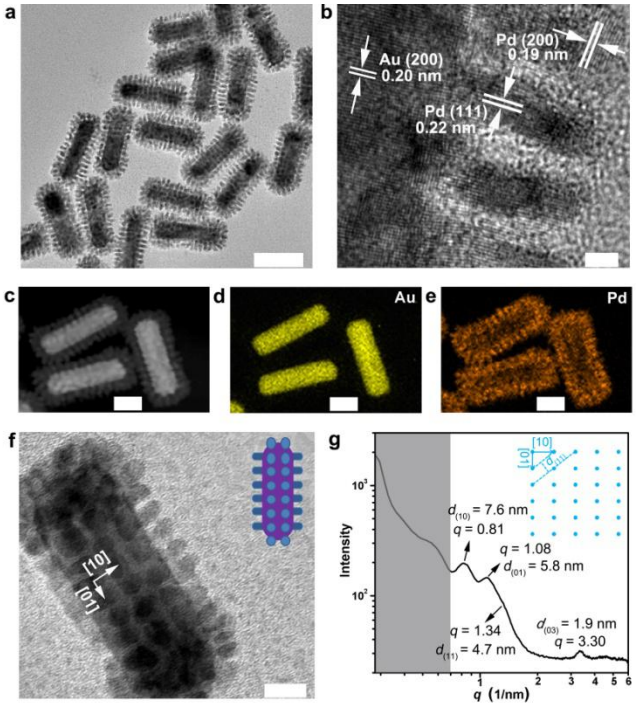

Figure 1. Characterization of Au@Pd SSs. (a) Typical TEM image of Au@Pd SSs, scale bar is 50 nm. (b) HRTEM image of Au@Pd SSs, scale bar is 2 nm. (c) HAADF-STEM image of Au@Pd SSs, scale bar is 20 nm. (d,e) EDX mapping images of element Au and Pd, respectively, scale bars are 20 nm. (f) TEM image of single Au@Pd SS, and the arrows clearly indicate the periodic arrangement of Pd nanoarray along the transverse [10] and longitudinal [01] axes of Au NR, respectively, scale bar is 10 nm. (g) One dimensional SAXS profile of Au@Pd SSs in aqueous solution, and interference in grey-colored region is ascribed to the positional correlations of CPC micelles. Inset in (g) presents 2D simple tetragonal lattice of superstructure.

To uncover the ordered superstructure feature, TEM imaging on single Au@Pd SSs was taken (Fig. 1f).

Evidently, Pd particles with diameter of 3.8 ± 0.1 nm (Fig. S1d) adopt an ordered two-dimensional (2D) array, that is, simple tetragonal arrangement along the directions paralleling to the transverse [10] and longitudinal [01] axes of Au NRs, respectively. The center-to-center spacing between neighboring Pd particles along [10] and [01] directions is 7.7 ± 0.3 and 5.8 ± 0.3 nm based on the statistic measurement on TEM images (Fig. S1e,f). More importantly, beside above microscopic observation on the TEM substrates, such ordered superstructures in bulk solution can be unambiguously discerned by the small angle X-ray scattering (SAXS) profile. As seen from Fig. 1g, the interference below q range of 0.7 nm^{-1} (grey colored region) corresponds to the positional correlation of CPC micelles[16], which also appears in the case of disordered Au@Pd nanostructures (Fig. S6). In the range of q > 0.7 nm^{-1}, the peaks centered at 0.81, 1.08, 1.34 and 3.30 nm^{-1} are assigned to the (10), (01), (11) and (03) faces of the Pd superstructures on Au NR surfaces, respectively, based on the 2D simple tetragonal model (Fig. 1g, inset). Consequently, the lattice period of (10) and (01) is 7.6 and 5.8 nm calculated from the SAXS data, which is highly consistent with the inter-spacing between Pd particles deduced from TEM imaging (Fig. S1e,f). It is worth mentioning that to our knowledge, this the first reported freestanding hetero-superstructure featured with regular NP arrangement on the surface of another type of NP.

Formation Mechanism of Au@Pd SSs. Seed-mediated growth is a general method to synthesize the hybrid nanostructures via overcoming possible self-nucleation process in solution[17]. One basic operation in this method is to employ a modest or low temperature to reduce the reaction rate for avoiding burst self-nucleation[17]. However, the result found in this work seems counter-intuitive. Under the identical experimental condition with different reaction temperature, the Au@Pd SSs without self-nucleated Pd NPs are obtained only at relatively high temperature of 65°C (Fig. S3a), whereas the separated branched Pd NPs appear and grow when the temperature decreases to 45°C and 25°C (Fig. S3b,c). To disclose the underlying mechanism, dynamic light scatting (DLS) technique was used to monitor the size variation of structure directing agent CPC in solution. As for pure 10 mM CPC in solution, a sharp peak arises at around 0.7 nm at 25°C (Fig. S4a), indicative of its good solubility. After adding Na_2PdCl_4 precursor, the resultant solution becomes turbid (inset in Fig. S4b), suggesting formation of large $[CPC^+]_2 \cdot [PdCl_4^{2-}]$ micelles via electrostatic attraction[16]. The formation of micelles is also evidenced by the obviously increased sizes and broadened size distribution measured by DLS (Fig. S4b). These $[CPC^+]_2 \cdot [PdCl_4^{2-}]$ aggregates strictly confine diffusion and reduction of Pd precursor during synthesis, thus preventing heterogonous nucleation and growth of Pd particles onto Au NR seeds. With increasing the reaction temperature, the above micelles are gradually collapsed and dissolved in solution, which are verified by the decreased sizes and narrowed size distribution at 45°C and 65°C (Fig. S4c,d) as well as appearance of the transparent solution (insets in Fig. S4c,d). As a result, free Pd precursors in solution are easily diffused and reduced onto the Au NR surfaces for formation of the Au@Pd SSs at 65°C.

To further clarify the formation mechanism involved in the Au@Pd SSs, their evolution process was monitored by time-dependent TEM imaging. After adding the reduction agent ascorbic acid immediately, both isolated Pd clusters and small Pd domains attaching on the Au NRs are discerned (Fig. S5a), implying simultaneous occurrence of both homo-nucleation and hetero-nucleation of Pd at the initiate stage. As the evolution proceeding, isolated Pd clusters disappear quickly along with increment of the separated Pd domains on Au NRs in both number and length (Fig. S5b,c), suggesting that Pd nanoarrays of the Au@Pd SSs are likely formed at the cost of small Pd clusters via the Ostwald ripening process[18]. Notably, Pd nanoarrays exhibit the ordered arrangement on the surfaces of Au NRs within 2 min reaction (Fig. S5d) and finally evolve into the Au@Pd SS (Fig. S5e,f).

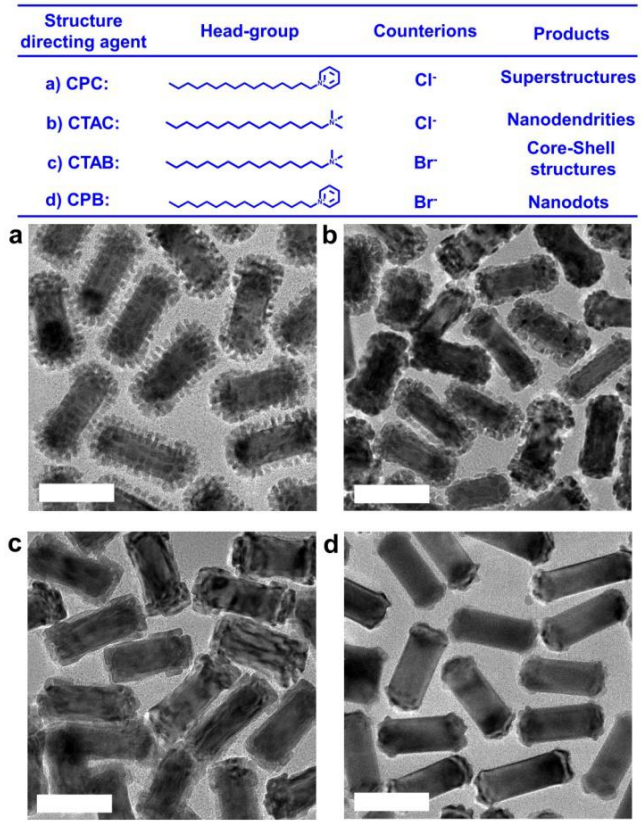

Figure 2. Products formed by different structure directing agent. TEM images of products prepared with (a) CPC, (b) CTAC, (c) CPB, (d) CTAB as the structure directing agent, under identical reaction conditions. Scale bars in (a-d) are 50 nm.

The role of surfactant on formation of the superstructures is two folds: the capping agent to stabilize colloidal NPs and the soft template (micelle or lyotropic liquid crystal) to direct formation of the well-defined structures[19]. Many contrast experiments with varied surfactants of similar molecular structure were carried out

to elucidate the specificity in preparation of the Au@Pd SSs. Firstly, the aromatic pyridinium headgroup of CPC is replaced with linear ammonium, namely CTAC, as the structure directing agent. Au@Pd NDs with Pd NPs randomly attached on the surfaces of Au NRs are produced (Fig. 2b), and is further proved by absence of distinct peaks in SAXS profile (Fig. S6a). This result shows that the pyridinium headgroup of CPC is crucial for directing formation of the ordered Pd nanoarrays via self-organization of surfactant molecules on Au NRs surfaces, which originates from the stronger polarizability[20] and additional aromatic π - π stacking interaction of pyridinium headgroup compared to CTAC. Beside the cationic part, appropriate anion moiety of surfactant is also important for formation of the Au@Pd SSs. When hexadecylpyridinium bromide (CPB) is used instead of CPC, products of Au NRs with tiny Pd dots attaching at the ends are obtained (Fig. 2d); meanwhile, the Au@Pd CSs with continuous Pd thin shells are prepared (Fig. 2c) when CTAB is employed. These results are in agreement with previous reports using bromide containing surfactants, in which solid Pd shells are facilely formed at slow growth rate caused by the stronger bonding ability of Br^- on Pd surface and the suppressed reduction potential of metal precursors[21]. After conducting more control experiments, we found that the concentration of CPC used in synthesis also influenced the quality of the obtained Au@Pd SSs. As displayed in Fig. S7a, low concentration of CPC (e.g. 1 mM) solution is not adequate to produce the Au@Pd SSs, while excessive surfactant, e.g. fivefold and tenfold larger than the standard concentration of 10 mM, gives rise to the shrunk Pd branches and even continuous Pd domains (Fig. S7c,d). This phenomenon is resulted from the suppressed growth rate of Pd with high concentration of CPC, which is analogous to the case using CTAB as the surfactant.

SPR Characteristics of Au@Pd SSs. Since the SPR characteristics of noble metal nanostructures are highly sensitive to their component, shape and dielectric constant of surrounding environment, the Au@Pd SSs with integrated composition and controlled structure offer us feasible ways to manipulate their optical properties for desired applications. For instance, when Au NRs with AR of 2.6 ± 0.3 (Fig. 3a) are chosen as the seeds, distinct SPR absorption band could be inherited after formation of the Au@Pd SSs (Fig. 3f), in contrast to seriously damped or even vanished peak reported in Au@Pd CSs[12b, 12c]. This merit is benefitted from the discontinuous arrangement[12c] and antenna effect[22] of ultra-sharp Pd arrays in the Au@Pd SSs. More importantly, the longitudinal SPR (LSPR) peak of Au@Pd SSs might be gradually tuned from 750 to 850 nm by simply increasing Pd precursors (Fig. 3f). Simultaneously, the average length of Pd nanoarrays on Au NR surfaces (Fig. 3b-d) is altered from 3.2 ± 0.4 to 6.9 ± 0.6 nm (Fig. S8a-c) accompanied with increasing surface density. As expected, further addition of Pd precursors in the growth solution could not lead to obvious change in both morphology (Fig. 3e and Fig. S8d) and SPR absorption property (Fig. 3f) of the products, which represents the complete formation of the Au@Pd SSs with intact Pd nanoarrays.

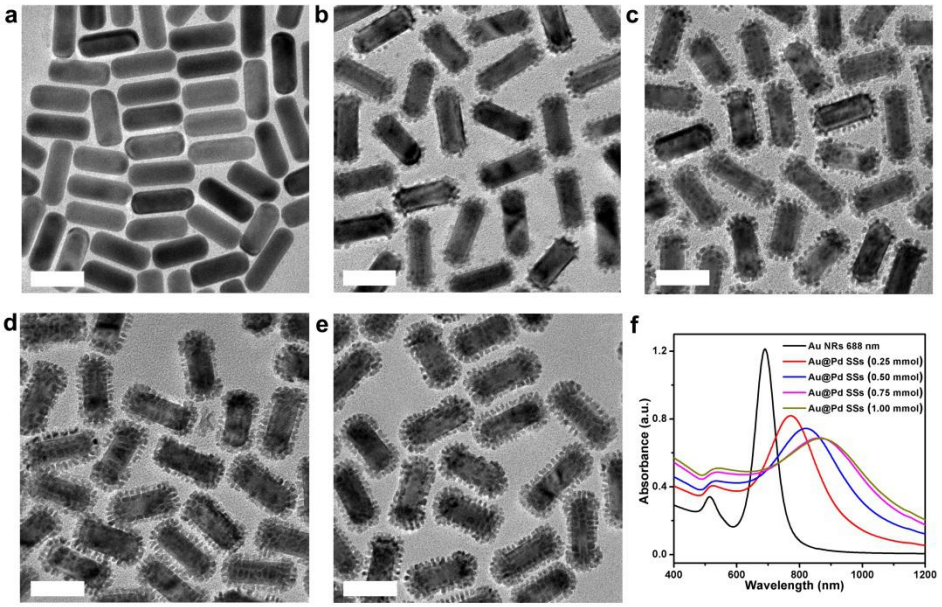

Figure 3. Tunable SPR properties of Au@Pd SSs**.** (a) TEM image of Au NR seeds. TEM images of Au@Pd SSs prepared with (b) 0.25 μmol, (c) 0.50 μmol, (d) 0.75 μmol and (e) 1.00 μmol Na_2PdCl_4 precursors. (f) Vis-NIR spectra of Au NRs and Au@Pd SSs with increasing Na_2PdCl_4 amount. Scale bars in (a-e) are 50 nm.

Alternatively, SPR band of the Au@Pd SSs might be adjusted to near infrared (NIR) region by increasing AR of the Au NRs. Fig. S9 and S10 demonstrate that the LSPR peaks of the Au@Pd SSs red shift from 866 to 1000 nm when AR of the Au NR seeds increases from 2.6 ± 0.3 to 3.5 ± 0.3, thus enabling the Au@Pd SSs possessing strong

absorption in both visible (transverse SPR, TSPR) and NIR region (LSPR). Evidently, one could easily tune the optical absorption of the Au@Pd SSs to the required wavelength or maximizes their absorption in whole Vis-NIR region for efficient utilization of solar energy.

In addition to the Au@Pd SSs, the SPR characteristics of some classic nanostructures, which includes Au@Pd NDs, Au@Pd CSs, bare Au NRs, porous Pd NPs as well as simple mixture of Au NRs and porous Pd NPs (Fig. S11), are also investigated. It is noticed that in order to make the comparison on plasmon-induced hot electrons meaningful, both the weight of Au and/or Pd in each sample (Tab. S1) and its plasmon absorption band (Fig. S11f) are controlled to be similar in all the experiments.

Generation of hot electrons from the ground state to high energy state in noble metal nanostructures is dominated by the electric field induced by plasmon, and stronger field will give rise to more hot electrons[1b, 23]. Hence, finite-difference time-domain (FDTD) method is employed to calculate the $|\mathbf{E}|/|\mathbf{E}_0|$ distribution contours of different Au@Pd nanostructures and bare Au NRs, where $|\mathbf{E}|$ and $|\mathbf{E}_0|$ denote the enhanced and incident electric field, respectively. As demonstrated in Fig. 4a, unlike the strong $|\mathbf{E}|/|\mathbf{E}_0|$ distribution at both ends of bare Au NRs, the Au@Pd CSs exhibit negligible electric field enhancement caused by the serious plasmon shielding effect of continuous Pd shells. When this continuous Pd obstruction is replaced with discrete Pd dendrites in case of the Au@Pd NDs, the $|\mathbf{E}|/|\mathbf{E}_0|$ around their surface is largely enhanced with a maximum value $|\mathbf{E}_{max}|/|\mathbf{E}_0|$ of 16 by allowing inside Au NR core being partially excited. Very impressively, the Au@Pd SSs possess further improvement of $|\mathbf{E}_{max}|/|\mathbf{E}_0|$ (up to 23) and more extensive field distribution compared with the Au@Pd NDs, resulting from ordered open structure of Pd nanoarrays[12c] as well as their strong plasmonic antenna effect[22]. In brief, the Au@Pd SSs are of the strongest field enhancement among diverse Au@Pd nanostructures (Fig. 4c), endowing their superior ability of hot electron production.

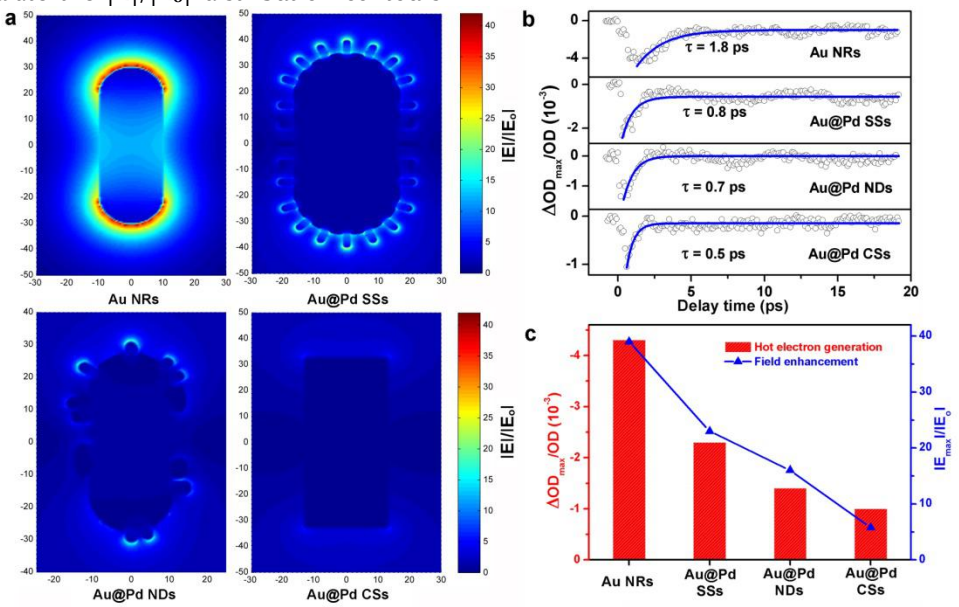

Figure 4. Characterization of hot electrons in Au@Pd nanostructures. (a) Comparison of electric field enhancement ($|\mathbf{E}|/|\mathbf{E}_0|$) contours of bare Au NRs, Au@Pd SSs, Au@Pd NDs and Au@Pd CSs at LSPR excitation. (b) Single-wavelength dynamics of bare Au NRs, Au@Pd SSs, Au@Pd NDs and Au@Pd CSs probed at each LSPR band. The blue curves are fitting plots taking into account of electron-phonon thermalization with corresponding time constant of τ. (c) Correlation between $\Delta OD_{max}/OD$ and $|\mathbf{E}_{max}|/|\mathbf{E}_0|$ among different Au NRs based nanostructures.

Except for theoretic prediction, the generation and dynamics of hot electrons in the Au@Pd nanostructures were experimentally investigated by transient absorption (TA) measurement[8b, 24]. Upon pulse excitation, hot electrons are produced in all the measured nanostructures, accompanying with transient negative change in optical density (ΔOD) located at the LSPR band (Fig. S12)[8b, 24b]. Fig. 4b outlines the plot of ΔOD divided by its initiate optical density (OD) at the steady state, namely Δ OD/OD, against decay time for different nanostructures. Since ΔOD/OD represents the transient proportion of the excited hot electrons[8b, 24b], its maximal value ($\Delta OD_{max}/OD$) is an important index to assess the generation efficiency of hot electrons in diverse nanostructures. As expected, the Au@Pd SSs exert the highest hot electron generation efficiency among three Au@Pd nanostructures but lower than that of bare Au NRs (Fig. 4c). Noteworthily, the good correlation between Δ OD_{max}/OD and $|\mathbf{E}_{max}|/|\mathbf{E}_0|$ among diverse nanostructures distinctly reveals that the stronger field enhancement effect is responsible for production of more hot electrons.

Another important finding in the TA spectroscopy is about the dynamics of hot electrons, which are tracked by the transient ΔOD/OD kinetics in picoseconds. Seen from Fig. 4b, the fast exponential decay of Δ OD/OD is

attributed to the electron-phonon relaxation of hot electrons[8b, 24b], which leads to cooling into phonon modes. The bare Au NRs possess a time constant (τ) of 1.8 picosecond (ps), which is very close to the typical τ_{e-p} value of Au NRs reported in literatures[24]. Obviously, the decay of hot electrons in each Au@Pd nanostructures is much faster compared with that of bare Au NRs, which should be ascribed to the much larger electron-phonon coupling constant of Pd (8.7×10^{17} W m^{-3} K^{-1})[25] with respect to Au (3.0×10^{16} W m^{-3} K^{-1})[26] since the reveserly proportional relationship between this constant with the decay time[27]. Nevertheless, the Au@Pd SSs display longer decay time (0.8 ps) of hot electrons compared with Au@Pd NDs (0.7 ps) and Au@Pd CSs (0.5 ps), which should be attributed to the smallest Au/Pd interface in the Au@Pd SSs among those Au@Pd nanostructures as hot electrons would fast decay at these Au/Pd interfaces. Hence, Au@Pd SSs would provide longer time window for additional hot electron transfer process, for example, activating the adsorbates for promotion of chemical transformation. Altogether, Au@Pd SSs are supposed to be ideal plasmon-enhanced catalysts among varied nanostructures because of the following merits: controllable integration of strong plasmon absorption and excellent catalytic activity, effective generation of hot electrons due to large field enhancement, and long decay time of hot electrons for adsorbates activation.

Plasmon-enhanced catalytic activity of Au@Pd SSs. As discussed above, both generation efficiency and decay time of hot electrons in nanostructures might have large influence on the plasmon-enhanced catalytic activity. In order to distinguish individual contribution of each effect experimentally, we intend to select two types of classic hot-electron valuation reactions[28] with different time scales for investigation: (1) oxygen activation with much faster bond dissociation event (50 fs)[28a] than electron-phonon dissipation of hot electrons (500-800 fs in Fig. 4b), and (2) carbon-carbon coupling reaction of similar dissociation rate (400 fs)[29] with this decay. It needs to be stressed that both chosen catalytic reactions on Pd surfaces have many important applications. For examples, activation of molecular oxygen (O_2) to form ROS plays irreplaceable roles in physiological processes[30] and services as benign and strong oxidants for synthesis of fine chemicals[31]; meanwhile carbon-carbon coupling reaction like Suzuki-Miyaura coupling is a powerful tool

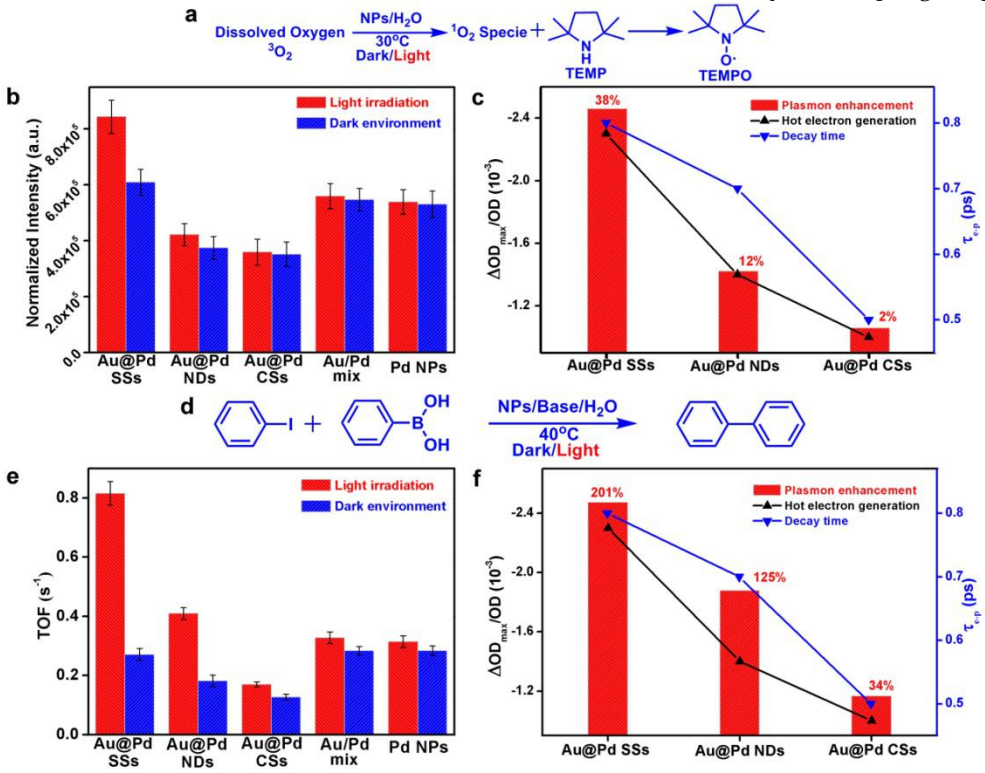

Figure 5. Plasmon-enhanced catalytic performances of Au@Pd nanostructures. (a) Scheme of evaluation of $^1O_2$ specie activated by varied nanostructures by using ESR method with TEMP as trapping agent. (b) Normalized ESR intensity of varied nanostructures under both dark environment (blue bars) and light irradiation (red bars), and error bars represent the standard derivation of three parallel tests. (c) Correlations between plasmon enhanced catalytic activity of diverse Au@Pd nanostructures with hot electron generation ($\Delta OD_{max}/OD$) and decay time (τ_{e-p}), respectively. (d) Scheme of Suzuki-coupling reaction catalyzed by varied nanostructures. (e) TOF value achieved by varied nanostructures under both dark environment (blue bars) and light irradiation (red bars), and error bars represent the standard derivation of three parallel test. (f) Correlations between plasmon enhanced catalytic activity of diverse Au@Pd nanostructures with hot electron generation ($\Delta OD_{max}/OD$) and decay time (τ_{e-p}), respectively.

in modern organic synthesis and has been broadly employed in pharmaceuticals[32] and functional materials[33].

In all the tests, the catalytic activity of varied nanostructures including Au@Pd SSs, Au@Pd NDs,

Au@Pd CSs, bare Au NRs, porous Pd NPs, and the mixture of Au NRs and porous Pd NPs was assessed parallelly. Note that the continuous light irradiation on the nanostructures was implemented by a Xe lamp with a 510 nm long-pass filter (Fig. S13) and a low energy of 0.7 W cm^{-2}, in order to avoid exciting their interband transition. Since the photothermal effect of plamonic NPs possibly results in localized high temperature for promoting reaction on their surfaces, we estimate the temperature rise from light irradiation based on previous calculation method[34]. As for Au NRs with AR of 3.0, the final temperature difference (ΔT) is about 1.7×10^{-4} K under irradiation with light power of 0.7 W cm^{-2} in water (details are available in Supporting Information), which is comparable with a result of $\Delta T = 1.5 \times 10^{-4}$ K reported in literature[35]. Evidently, such negligible difference allows us excluding possible photothermal contribution by strictly controlling the incubation temperature of thermal bath for the experiments under both dark condition and light irradiation.

As for O_2 activation by various nanostructures, electron spin resonance (ESR) spectroscopy coupled with trapping agents is used to identify and quantify ROS products[15, 36]. By using 2,2,6,6-tetramethyl-4-piperidine (TEMP) as special trapping agent (Fig. 5a), triplet line with equal intensity and a hyperfine splitting constant of $\alpha_N = 16.0$ G, corresponding to a characteristic singlet oxygen ($^1O_2$) adduct (4-oxo-2,2,6,6-tetramethylpiperidine-N-oxyl, TEMPO)[15, 36a], are clearly observed from the ESR spectra of all Pd containing samples but no discernable signals in the test of bare Au NRs (Fig. S14), which suggests that singlet oxygen species ($^1O_2$) is produced on active Pd sites[37]. Further evidence on production of $^1O_2$ species is offered by the seriously quenched ESR signal (Fig. S15) via using histidine as a specific $^1O_2$ scavenger[38]. Based on the normalized ESR intensity (Fig. 5b, blue bars), the activity of Au@Pd SSs under dark environment is 1.6 and 1.8 fold than that of disordered Au@Pd NDs and solid Au@Pd CSs, respectively, and even higher than that of porous Pd NPs as well as their mixture with Au NRs, which is benefitted from much more exposed active sites and richer Pd corners/edges created by the regular and ultra-sharp Pd nanoarrays of Au@Pd SSs. Upon light irradiation (Fig. 5b, red bars), the catalytic activity of porous Pd NPs, bare Au NRs and their simple mixture keeps unchanged with respect to that under dark environment, which is reasonable due to lack of generation or injection of hot electrons. As comparison, the light enhanced catalytic activity of Au@Pd SSs is up to 38%, much higher than 12% of Au@Pd NDs and nearly no increment of Au@Pd CSs (Fig. 5c). In regard of Suzuki-Miyaura coupling between iodobenzene and benzeneboronic acid (Fig. 5d), hot electron effect is also found to largely promote the reaction. As shown in Fig. 5e,f, Au@Pd SSs have the largest turnover frequency (TOF) value among all the tested catalysts under light irradiation, as well as much stronger plasmon enhancement (201%) compared with Au@Pd NDs (125%) and Au@Pd CSs (34%). Notably, such prominent plasmon enhancement property of Au@Pd SSs in oxygen activation and carbon-carbon coupling reaction should be attributed to their structure superiority, as both composition weight and absorption band of these Au@Pd nanostructures are controlled to be similar (Tab. S1 and Fig. S11f).

Since the photothermal effect in our case is negligible according to our theory estimation, which is further confirmed by the clearly linear relationships[39] between the reaction rate and incident light intensity in Fig. S16. Moreover, the good consistency between the wavelength-dependent performance and corresponding absorption spectrum shown in Fig. S17 indicates that the SPR absorption of Au@Pd nanostructures indeed affects the two catalytic reactions. Consequently, the much higher photocatalytic activity of Au@Pd SSs is mainly ascribed to their superstructure-determined stronger generation ability and longer decay time of hot electrons in comparison with these of conventional Au@Pd nanostructures (NDs and CSs). Typically, hot electrons of high energy would engage the catalytic reaction via the injection of them from the nanostructures into the anti-bonding orbital of surfaces adsorbates sequentially facilitating the specific bond dissociation process and thereby promoting the catalytic rate of reaction. As for oxygen activation by plasmonic NPs, hot electrons could be injected into the anti-bonding ($2\pi^*$) orbital of molecular oxygen adsorbed on surface of NPs upon plasmonic absorption, elongating the oxygen-oxygen bond and activating the following chemical reaction[28a-c]. Considering the fact that the timescale of O_2 dissociation event (50 fs)[28a] is much faster than that of electron-phonon relaxation (500-800 fs) in these Au@Pd nanostructure, efficient hot electron transfer from Pd into the adsorbed oxygen orbitals is permitted for prompting the activation reaction. Thus, the obtained plasmon enhancement among diverse Au@Pd nanostructures should be mainly determined by the efficiency of hot electron generation, as verified by good correlation of plasmon enhancement ratio with $\Delta OD_{max}/OD$ value (black curve in Fig. 5c). Similarly, the injection of hot electrons into the lowest unoccupied molecular orbital (LUMO) of iodobenzene molecule adsorbed on Pd surface could easily take place and then promoting the dissociation of the C-I bond[28d-f]. In contrast to oxygen activation, nice correlation of hot electron decay time with plasmon enhancement ratio is discerned in case of coupling reaction (blue curve in Fig. 5d), indicative of domination of hot electrons transfer during this reaction. This is because the timescale of dissociation of iodobenzene (400 fs)[29], the key step in the coupling reaction[40], is slow enough and has to compete with the electron-phonon dissipation route (500-800 fs)[41]. In combined, the distinguished role of hot electrons generation and lifetime in this work would offer new route to achieve optimal plasmon-enhanced catalyst via elaborate nanostructure design and reasonable reaction selection.

Conclusion

The two-fold benefit from the structure advantages of Au@Pd SSs largely facilitates the plasmon-enhanced catalysis. The ordered open structure of Pd nanoarrays with strong plasmonic antenna effect maximizes the field enhancement from Au NRs, thus promoting oxygen activation via improving the hot electron generation; while the vertical organization of Pd arrays with small contact on Au NRs minimizes the electron-phonon relaxation, therefore enhancing carbon-carbon coupling reaction through slowing the hot electron decay. This work demonstrates the genuine superiority of the hetero-superstructures in the important catalytic reactions, which will offer useful guidelines to design and construct high performance plasmon-based catalysts, sensors and devices in the coming future.

ASSOCIATED CONTENT

Supporting Information. Additional synthesis methods, supplementary figures and table are available free of charge via the Internet at http://pubs.acs.org.

AUTHOR INFORMATION

Corresponding Author

*wangxl@nanoctr.cn

*zytang@nanoctr.cn

Author Contributions

‡J.G. and Y.Z. contributed equally.

Notes

The authors declare no competing financial interests.

ACKNOWLEDGMENT

The authors acknowledge financial support from National Key Basic Research Program of China (2014CB931801 and 2016YFA0200700, Z.T.), National Natural Science Foundation of China (21475029 and 91427302 (Z.T.), 21673053 (X.W.)), Frontier Science Key Project of the Chinese Academy of Sciences (QYZDJ-SSW-SLH038, Z.T.), Instrument Developing Project of the Chinese Academy of Sciences (YZ201311, Z.T.), CAS-CSIRO Cooperative Research Program (GJHZ1503, Z.T.), "Strategic Priority Research Program" of Chinese Academy of Sciences (XDA09040100, Z.T.) and K.C.Wong Education Foundation.

REFERENCES

(1) (a) Linic, S.; Christopher, P.; Ingram, D. B., *Nat. Mater.* **2011,** *10*, 911; (b) Linic, S.; Aslam, U.; Boerigter, C.; Morabito, M., *Nat. Mater.* **2015,** *14*, 567; (c) Liz-Marzan, L. M.; Murphy, C. J.; Wang, J., *Chem. Soc. Rev.* **2014,** *43*, 3820; (d) Smith, J. G.; Faucheaux, J. A.; Jain, P. K., *Nano Today* **2015,** *10*, 67; (e) Collins, G.; Holmes, J. D., *Adv. Mater.* **2016,** *28*, 5689; (f) Park, J. Y.; Baker, L. R.; Somorjai, G. A., *Chem. Rev.* **2015,** *115*, 2781.

(2) (a) Mukherjee, S.; Libisch, F.; Large, N.; Neumann, O.; Brown, L. V.; Cheng, J.; Lassiter, J. B.; Carter, E. A.; Nordlander, P.; Halas, N. J., *Nano Lett.* **2012,** *13*, 240; (b) Mukherjee, S.; Zhou, L.; Goodman, A. M.; Large, N.; Ayala-Orozco, C.; Zhang, Y.; Nordlander, P.; Halas, N. J., *J. Am. Chem. Soc.* **2014,** *136*, 64; (c) Xiao, Q.; Liu, Z.; Bo, A.; Zavahir, S.; Sarina, S.; Bottle, S.; Riches, J. D.; Zhu, H., *J. Am. Chem. Soc.* **2015,** *137*, 1956; (d) Aslam, U.; Chavez, S.; Linic, S., *Nat. Nanotech.* **2017,** *doi: 10.1038/NNANO.2017.131*; (e) Zheng, Z.; Tachikawa, T.; Majima, T., *J. Am. Chem. Soc.* **2014,** *136*, 6870.

(3) (a) Bonn, M.; Funk, S.; Hess, C.; Denzler, D. N.; Stampfl, C.; Scheffler, M.; Wolf, M.; Ertl, G., *Science* **1999,** *285*, 1042; (b) Xiao, Q.; Sarina, S.; Waclawik, E. R.; Jia, J.; Chang, J.; Riches, J. D.; Wu, H.; Zheng, Z.; Zhu, H., *ACS Catal.* **2016,** *6*, 1744; (c) Zhang, X.; Li, X.; Zhang, D.; Su, N. Q.; Yang, W.; Everitt, H. O.; Liu, J., *Nat. Commun* **2017,** *8*, 14542; (d) Robatjazi, H.; Zhao, H.; Swearer, D. F.; Hogan, N. J.; Zhou, L.; Alabastri, A.; McClain, M. J.; Nordlander, P.; Halas, N. J., *Nat. Commun.* **2017,** *8*, 27.

(4) Marimuthu, A.; Linic, S., *Science* **2013,** *339*, 1590.

(5) (a) Liu, K.; Ahmed, A.; Chung, S.; Sugikawa, K.; Wu, G.; Nie, Z.; Gordon, R.; Kumacheva, E., *ACS Nano* **2013,** *7*, 5901; (b) Hu, Y.; Li, Z.; Sun, Y., *Catal. Today* **2014,** *225*, 177; (c) Wang, C.; Astruc, D., *Chem. Soc. Rev.* **2014,** *43*, 7188; (d) Scarabelli, L.; Hamon, C.; Liz-Marzán, L. M., *Chem. Mater.* **2017,** *29*, 15.

(6) (a) Li, B.; Wen, X.; Li, R.; Wang, Z.; Clem, P. G.; Fan, H., *Nat. Commun.* **2014,** *5*, 4179; (b) Klinkova, A.; Thérien-Aubin, H.; Gagnon, B.; Gang, O.; Walker, G. C.; Ahmed, A.; Nykypanchuk, D.; Choueiri, R. M.; Muntyanu, A.; Kumacheva, E., *Nano Lett.* **2014,** *14*, 6314; (c) Polavarapu, L.; Zanaga, D.; Altantzis, T.; Rodal-Cedeira, S.; Pastoriza-Santos, I.; Pérez-Juste, J.; Bals, S.; Liz-Marzán, L. M., *J. Am. Chem. Soc.* **2016,** *138*, 11453.

(7) Kale, M. J.; Avanesian, T.; Xin, H.; Yan, J.; Christopher, P., *Nano Lett.* **2014,** *14*, 5405.

(8) (a) Link, S.; El-Sayed, M. A., *J. Phys. Chem. B* **1999,** *103*, 8410; (b) Link, S.; Burda, C.; Mohamed, M.; Nikoobakht, B.; El-Sayed, M., *Phys. Rev. B* **2000,** *61*, 6086.

(9) (a) Wu, K.; Chen, J.; Mcbride, J. R.; Lian, T., *Science* **2015,** *349*, 632; (b) Shi, R.; Cao, Y.; Bao, Y.; Zhao, Y.; Waterhouse, G. I. N.; Fang, Z.; Wu, L.-Z.; Tung, C.-H.; Yin, Y.; Zhang, T., *Adv. Mater.* **2017,** 10.1002/adma.201700803.

(10) (a) Gomes Silva, C.; Juárez, R.; Marino, T.; Molinari, R.; García, H., *J. Am. Chem. Soc.* **2011,** *133*, 595; (b) Peerakiatkhajohn, P.; Butburee, T.; Yun, J. H.; Chen, H. J.; Richards, R. M.; Wang, L. Z., *J. Mater. Chem. A* **2015,** *3*, 20127; (c) Xiao, F.-X.; Zeng, Z.; Liu, B., *J. Am. Chem. Soc.* **2015,** *137*, 10735.

(11) Zhang, Y.; Yam, C.; Schatz, G. C., *J. Phys. Chem. Lett.* **2016,** *7*, 1852.

(12) (a) Feng, L.; Wu, X.; Ren, L.; Xiang, Y.; He, W.; Zhang, K.; Zhou, W.; Xie, S., *Chem.-Eur. J.* **2008,** *14*, 9764; (b) Lee, Y. W.; Kim, M.; Kim, Z. H.; Han, S. W., *J. Am. Chem. Soc.* **2009,** *131*, 17036; (c) Chen, H. J.; Wang, F.; Li, K.; Woo, K. C.; Wang, J. F.; Li, Q.; Sun, L. D.; Zhang, X. X.; Lin, H. Q.; Yan, C. H., *ACS Nano* **2012,** *6*, 7162.

(13) Ye, X.; Gao, Y.; Chen, J.; Reifsnyder, D. C.; Zheng, C.; Murray, C. B., *Nano Lett.* **2013,** *13*, 2163.

(14) Huang, H.; Zhang, L.; Lv, Z.; Long, R.; Zhang, C.; Lin, Y.; Wei, K.; Wang, C.; Chen, L.; Li, Z. Y.; Zhang, Q.; Luo, Y.; Xiong, Y., *J. Am. Chem. Soc.* **2016,** *138*, 6822.

(15) Wen, T.; He, W.; Chong, Y.; Liu, Y.; Yin, J. J.; Wu, X., *Phys. Chem. Chem. Phys.* **2015,** *17*, 24937.

(16) Li, C.; Sato, T.; Yamauchi, Y., *Chem. Commun.* **2014,** *50*, 11753.

(17) (a) Wang, Y.; He, J.; Liu, C.; Chong, W. H.; Chen, H., *Angew. Chem. Int. Ed* **2015,** *54*, 2022; (b) Gilroy, K. D.; Ruditskiy, A.; Peng, H.-C.; Qin, D.; Xia, Y., *Chem. Rev.* **2016,** *116*, 10414.

(18) (a) Camargo, P. H. C.; Xiong, Y.; Ji, L.; Zuo, J. M.; Xia, Y., *J. Am. Chem. Soc.* **2007,** *129*, 15452; (b) Lim, B.; Kobayashi, H.; Yu, T.; Wang, J.; Kim, M. J.; Li, Z.-Y.; Rycenga, M.; Xia, Y., *J. Am. Chem. Soc.* **2010,** *132*, 2506.

(19) Zhang, J.; Li, C. M., *Chem. Soc. Rev.* **2012,** *41*, 7016.

(20) (a) Zhou, Y.; Antonietti, M., *Adv. Mater.* **2003,** *15*, 1452; (b) Kuang, D.; Brezesinski, T.; Smarsly, B., *J. Am. Chem. Soc.* **2004,** *126*, 10534.

(21) Wang, F.; Li, C. H.; Sun, L. D.; Xu, C. H.; Wang, J. F.; Yu, J. C.; Yan, C. H., *Angew. Chem. Int. Ed* **2012,** *51*, 4872.

(22) Schuller, J. A.; Barnard, E. S.; Cai, W.; Jun, Y. C.; White, J. S.; Brongersma, M. L., *Nat. Mater.* **2010,** *9*, 193.

(23) Manjavacas, A.; Liu, J. G.; Kulkarni, V.; Nordlander, P., *ACS Nano* **2014,** *8*, 7630.

(24) (a) Park, S.; Pelton, M.; Liu, M.; Guyot-Sionnest, P.; Scherer, N. F., *J. Phys. Chem. C* **2007,** *111*, 116; (b) Jiang, Y.; Wang, H.-Y.; Xie, L.-P.; Gao, B.-R.; Wang, L.; Zhang, X.-L.; Chen, Q.-D.; Yang, H.; Song, H.-W.; Sun, H.-B., *J. Phys. Chem. C* **2010,** *114*, 2913.

(25) Wang, L.; Sagaguchi, T.; Okuhata, T.; Tsuboi, M.; Tamai, N., *ACS Nano* **2017,** *11*, 1180.

(26) Groeneveld, R. H. M.; Sprik, R.; Lagendijk, A., *Phys. Rev. B* **1995,** *51*, 11433.

(27) (a) Hartland, G. V., *Chem. Rev.* **2011,** 111, 3858; (b) Hodak, J. H.; Henglein, A.; Hartland, G. V., *J. Chem. Phys.* **2001,** 114, 2760.

(28) (a) Christopher, P.; Xin, H.; Linic, S., *Nat. Chem.* **2011,** 3, 467; (b) Huang, Y. F.; Zhang, M.; Zhao, L. B.; Feng, J. M.; Wu, D. Y.; Ren, B.; Tian, Z. Q., *Angew. Chem. Int. Ed.* **2014,** 53, 2353; (c) Sakamoto, H.; Ohara, T.; Yasumoto, N.; Shiraishi, Y.; Ichikawa, S.; Tanaka, S.; Hirai, T., *J. Am. Chem. Soc.* **2015,** *137*, 9324; (d) Wang, F.; Li, C.; Chen, H.; Jiang, R.; Sun, L.-D.; Li, Q.; Wang, J.; Yu, J. C.; Yan, C.-H., *J. Am. Chem. Soc.* **2013,** *135*, 5588; (e) Zhang, S.; Chang, C.; Huang, Z.; Ma, Y.; Gao, W.; Li, J.; Qu, Y., *ACS Catal.* **2015,** 5, 6481; (f) Xiao, Q.; Sarina, S.; Bo, A.; Jia, J.; Liu, H.; Arnold, D. P.; Huang, Y.; Wu, H.; Zhu, H., *ACS Catal.* **2014,** *4*, 1725.

(29) Cheng, P. Y.; Zhong, D.; Zewail, A. H., *Chem. Phys. Lett.* **1995,** *237*, 399.

(30) (a) Panikkanvalappil, S. R.; Mahmoud, M. A.; Mackey, M. A.; El-Sayed, M. A., *ACS Nano* **2013,** *7*, 7524; (b) Ge, J.; Lan, M.; Zhou, B.; Liu, W.; Guo, L.; Wang, H.; Jia, Q.; Niu, G.; Huang, X.; Zhou, H.; Meng, X.; Wang, P.; Lee, C. S.; Zhang, W.; Han, X., *Nat. Commun.* **2014,** 5, 4596; (c) Gao, X.; Gao, L., *ACS Nano* **2014,** *8*, 7260.

(31) (a) Kesavan, L.; Tiruvalam, R.; Rahim, M. H. A.; bin Saiman, M. I.; Enache, D. I.; Jenkins, R. L.; Dimitratos, N.; Lopez-Sanchez, J. A.; Taylor, S. H.; Knight, D. W.; Kiely, C. J.; Hutchings, G. J., *Science* **2011,** *331*, 195; (b) Lévesque, F.; Seeberger, P. H., *Angew. Chem. Int. Ed* **2012,** *51*, 1706; (c) Ghogare, A. A.; Greer, A., *Chem. Rev.* **2016,** *116*, 9994.

(32) Magano, J.; Dunetz, J. R., *Chem. Rev.* **2011,** *111*, 2177.

(33) Chen, L.; Yang, Y.; Jiang, D., *J. Am. Chem. Soc.* **2010,** *132*, 9138.

(34) Baffou, G.; Quidant, R.; Abajo, F. J. G. D., *ACS Nano* **2010,** *4*, 709.

(35) Huschka, R.; Zuloaga, J.; Knight, M. W.; Brown, L. V.; Nordlander, P.; Halas, N. J., *J. Am. Chem. Soc.* **2011,** *133*, 12247.

(36) (a) Moan, J.; Wold, E., *Nature* **1979,** *279*, 450; (b) Chiesa, M.; Giamello, E.; Che, M., *Chem. Rev.* **2010,** *110*, 1320.

(37) (a) Long, R.; Mao, K.; Ye, X.; Yan, W.; Huang, Y.; Wang, J.; Fu, Y.; Wang, X.; Wu, X.; Xie, Y.; Xiong, Y., *J. Am. Chem. Soc.* **2013,** *135*, 3200; (b) Long, R.; Huang, H.; Li, Y.; Song, L.; Xiong, Y., *Adv. Mater.* **2015,** *27*, 7025; (c) Cao, M.; Tang, Z.; Liu, Q.; Xu, Y.; Chen, M.; Lin, H.; Li, Y.; Gross, E.; Zhang, Q., *Nano Lett.* **2016,** *16*, 5298.

(38) Yamakoshi, Y.; Umezawa, N.; Ryu, A.; Arakane, K.; Miyata, N.; Goda, Y.; Masumizu, T.; Nagano, T., *J. Am. Chem. Soc.* **2003,** *125*, 12803.

(39) (a) Kim, S. M.; Lee, S. J.; Kim, S. H.; Kwon, S.; Yee, K. J.; Song, H.; Somorjai, G. A.; Park, J. Y., *Nano Lett.* **2013,** 13, 1352; (b) Li, K.; Hogan, N. J.; Kale, M. J.; Halas, N. J.; Nordlander, P.; Christopher, P., *Nano Lett.* **2017,** 17, 3710.

(40) Xue, L.; Lin, Z., *Chem. Soc. Rev.* **2010,** *39*, 1692.

(41) (a) Cavanagh, R.; King, D.; Stephenson, J.; Heinz, T., *J. Phys. Chem.* **1993,** *97*, 786; (b) Brongersma, M. L.; Halas, N. J.; Nordlander, P., *Nat. Nanotech.* **2015,** *10*, 25.

Table of Contents (TOC)

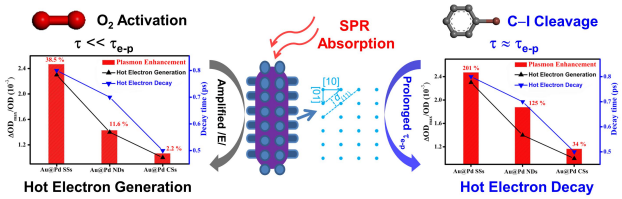

Supporting Information for

Boosting Hot Electrons in Hetero-Superstructures for Plasmon-Enhanced Catalysis

Jun Guo,[†,‡,§,‡] Yin Zhang,[†,‡,§,‡] Lin Shi,[†] Yanfei Zhu,[†,§] Megersa F. Mideksa,[†] Ke Hou,[†,‡,§] Wenshi Zhao,[†,§] Dawei Wang,[†] Meiting Zhao,[#] Xiaofei Zhang,[†] Jiawei Lv,[†] Jianqi Zhang,[†] Xiaoli Wang*[,†] and Zhiyong Tang*[,†]

[†]CAS Key Laboratory of Nanosystem and Hierarchical Fabrication, CAS Center for Excellence in Nanoscience, National Center for Nanoscience and Technology, Beijing 100190, P. R. China

[‡]Center for Nanochemistry, Peking University, Beijing 100871, P. R. China

[§]University of Chinese Academy of Sciences, Beijing 100049, P. R. China

[#]School of Materials Science and Engineering, Nanyang Technological University, Singapore 639798, Singapore

*Corresponding author E-mail: wangxl@nanoctr.cn; zytang@nanoctr.cn (Z.T)

Table of Contents

Part S1. Chemicals and Reagents

Tetrachloroauric acid hydrated ($HAuCl_4 \cdot 4H_2O$, analytical grade), sodium tetrachloropalladate (Na_2PdCl_4, 98%) and silver nitrate ($AgNO_3$, 99%) were purchased from Sinopharm. Hexadecylpyridinium chloride monohydrate (CPC, 99-102%) was bought from Sigma Aldrich. Hexadecyltrimethylammonium bromide (CTAB, > 98%), hexadecyltrimethylammonium chloride (CTAC, > 95%), sodium oleate (NaOL, > 97%), 2,2,6,6-tetramethyl-4-piperidonehydrochloride (TEMP, 95%) and 5,5-dimethyl-1-pyrroline n-oxide (DMPO, 97%) were achieved from TCI America. Hexadecylpyridiniumbromide monohydrate (CPB, 98%), sodium borohydride ($NaBH_4$, 98%), ascorbic acid (AA, 99%) and histidine (> 98%) were provided by Alfa Aesar. Hydrochloric acid (HCl, 37 wt%), sodium hydroxide (NaOH, analytical grade), ethanol (EtOH, analytical grade) and dichloromethane (CH_2Cl_2, analytical grade) were supplied by Beijing Chemical Reagent Company (China). All the chemicals were used as received without further purification.

Part S2. Supporting Information of Preparation and Characterization

Synthesis of Au NRs

Au NRs were synthesized by a seed-mediated growth method according to the literature with slight modification[S1]. Firstly, the seed solution was prepared by adding 0.25 mL of 10 mM $HAuCl_4$ into 5 mL of 200 mM CTAB solution, and then 0.6 mL of 10 mM freshly prepared $NaBH_4$ was quickly injected into the above solution under vigorous stirring. The obtained brownish yellow solution was aged at 30°C for 30 min before use.

To prepare the growth solution, 6 mL of 4 mM $AgNO_3$ and 250 mL $HAuCl_4$ were added into 250 ml aqueous solution containing 3.08 g CTAC and 0.77 g NaOL. The above mixture was kept at 30°C for 150 min under stirring. Subsequently, the colorless solution was introduced by 2 mL of 37 wt% HCl and stirred for another 15 min. Finally, 0.62 mL of 64 mM AA was added and vigorously stirred for 30 s, and then 0.4~0.6 mL of seed solution was quickly injected. The resultant solution was stirred for 1 min and left undisturbed at 30°C over night for growth. The aspect ratio (AR) of Au NRs could be tuned by changing the amount of seed solution.

The obtained Au NRs were isolated by centrifugation at 8000 rpm for 20 min and washed with pure water for 2 times to remove the excess surfactant. The precipitates were re-dispersed in 60 mL of pure water and served as seed solution for preparation of Au@Pd nanostructures.

Synthesis of Porous Pd NPs

Porous Pd NPs were synthesized according to literature[S2]. Briefly, 400 μL of 10 mM Na_2PdCl_4 was added into 5 mL of 10 mM CPC solution under stirring. The obtained mixture was heated to 40°C in the water bath, and 100μL of 100 mM AA was quickly injected with vigorous stirring for 1 min. After additional 240 min aging process, dark-brownish products were isolated by centrifugation at 8000 rpm for 10 min and washed with pure water for two times to remove the excess surfactant.

Supporting Figures for Characterization of Au@Pd SSs

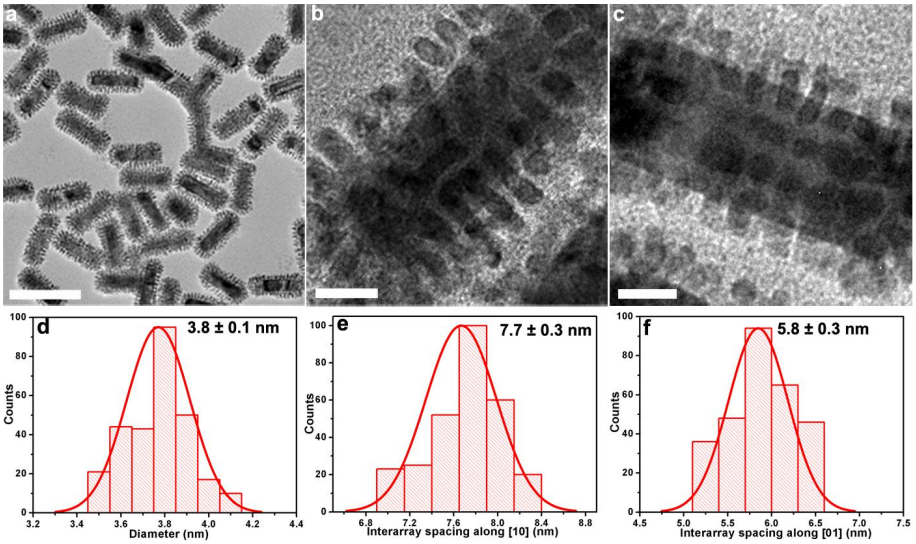

Figure S1. TEM characterization of Au@Pd SSs. (a) TEM image of Au@Pd SSs in large scale, scale bar is 100 nm. (b,c) TEM images of single Au@Pd SSs, scale bars are 10 nm. (d-f) Statistic histograms of (d) diameter of Pd nanoarrays, and inter-array spacing on Au@Pd SS surfaces along (e) [10] and (f) [01] directions.

As counted in Fig. S1, the average spacing of standing Pd nanoarrays along the transverse [10] and longitudinal [01] axis of Au NRs is 7.7 ± 0.3 and 5.8 ± 0.3 nm, respectively.

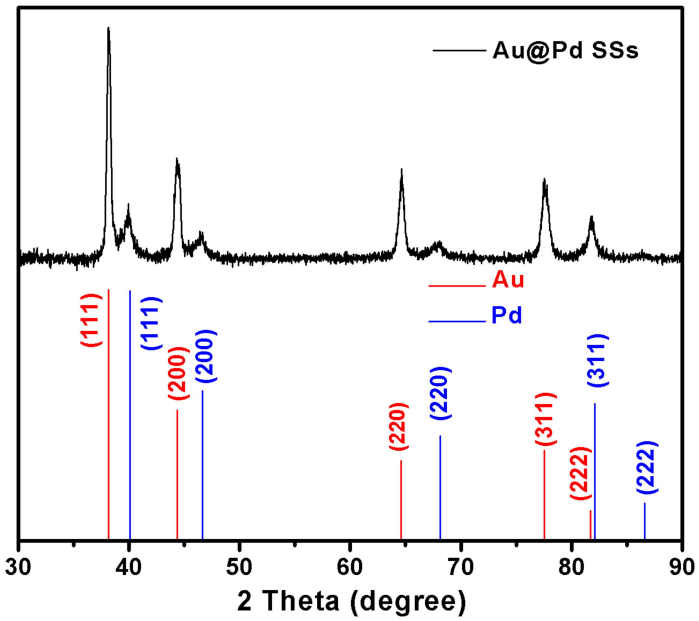

Figure S2. PXRD pattern of Au@Pd SSs. The corresponding peaks assigned by standard indexes of fcc Au (red lines, JCPDS no. 04-0784) and fcc Pd (blue lines, JCPDS no.46-1043).

As shown in Fig. S2, Au@Pd SSs are composed of fcc Au and fcc Pd without impurity phase.

Part S3. Supporting Information of Formation Mechanism Study

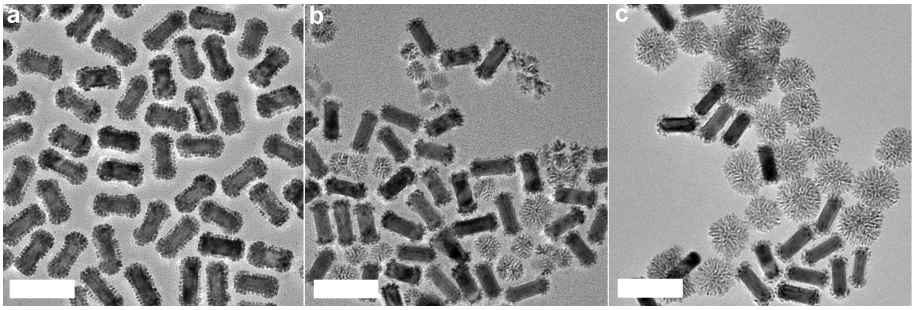

Figure S3. Temperature influence on production of Au@Pd SSs. (a-c) TEM images of products prepared at (a) 65°C, (b) 45°C and (c) 25°C, under other synthesis conditions identical to standard procedure. Unlabeled scale bars are 100 nm.

As products shown in Fig. S3, pure Au@Pd SSs could be prepared at 65°C, whereas more and more self-nucleated Pd NPs are produced when the incubation temperature decreases to 45°C and 25°C. This observation indicates that higher temperature is favorable for formation of hetero-nucleated Au@Pd SSs while low temperature benefits production of isolated Pd NPs.

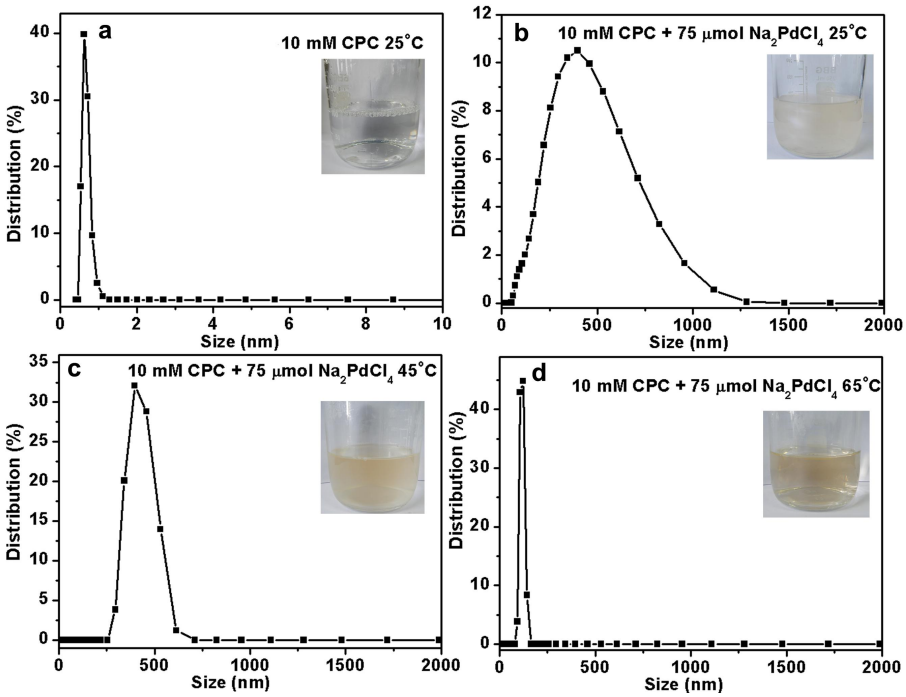

Figure S4. Temperature dependent DLS spectrum of $[CPC^+]_2 \cdot [PdCl_4^{2-}]$ micelles. (a-d) DLS spectrum of (a) 10 mM CPC solution at 25°C and after adding Na_2PdCl_4 precursors at (b) 25°C, (c) 45°C and (d) 65°C. Insets show corresponding photos of mixture.

In comparison to transparent CPC solution, the turbid suspension after adding Pd precursors (Na_2PdCl_4) together with obviously increased particle size (Fig. S4b) shows formation of $[CPC^+]_2 \cdot [PdCl_4^{2-}]$ micelles at 25°C, which strictly confine the nucleation and growth process of Pd to produce self-nucleated Pd NPs rather than Au@Pd SSs. With increasing temperature, the formed micelles are gradually collapsed or partially dissolved in solution, which are verified by their decreased size and narrowed size distribution at 45°C and 65°C (Fig. S4c,d) as well as appearance of transparent solution (insets in Fig. S4c,d). As a result, free Pd precursors are released, and thus Au@Pd SSs are obtained via hetero-nucleation and growth pathway.

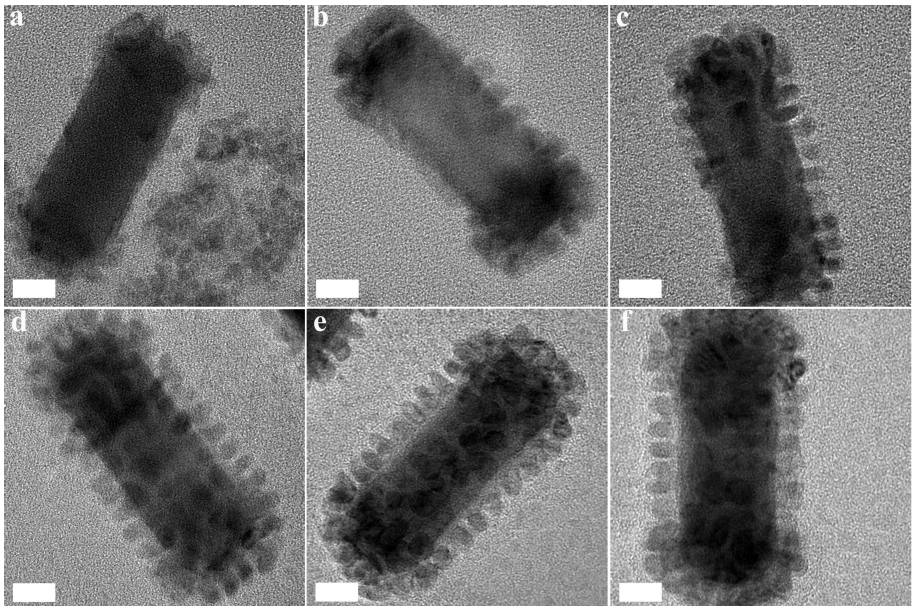

Figure S5. Evolution process of Au@Pd SSs. (a-f) HRTEM images of products after (a) immediately adding reductant, (b) growth for 0.5 min, (c) 1 min, (d) 2 min, (e) 5 min and (f) 0.5 h. Unlabeled scale bars are 10 nm.

Because of the fast reduction rate at high temperature (65^{o}C), both homo-nucleation and hetero-nucleation of Pd occur (Fig. S5a). Subsequently, small Pd clusters are dissolved accompanying with gradual growth of separated Pd nanoarrays on Au NR seeds via the Ostwald ripening process, which eventually gives rise to formation of highly regular Au@Pd SSs (Fig. S5b-f).

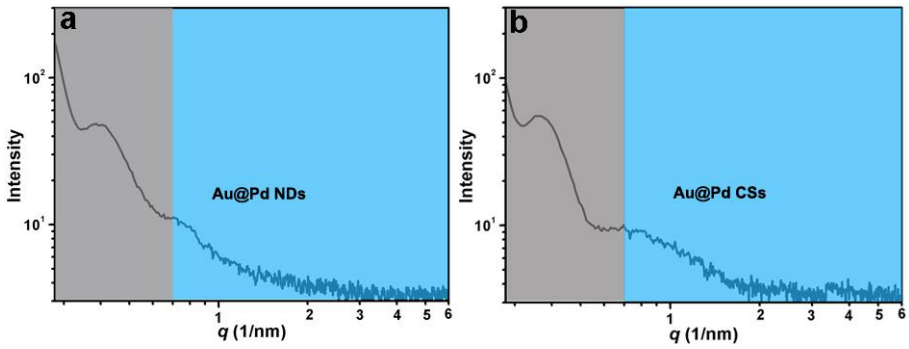

Figure S6. SAXS characterization of conventional Au@Pd nanostructures. (a,b) One dimensional SAXS plot of (a) Au@Pd NDs synthesized with CTAC and (b) Au@Pd CSs synthesized with CTAB as the structure directing agent, respectively.

Compared with Au@Pd SSs (Fig. 1g), the absence of relevant peaks in the blue regions of Fig. S6a,b indicates that the disordered deposition of Pd counterparts in Au@Pd NDs and Au@Pd CSs, respectively.

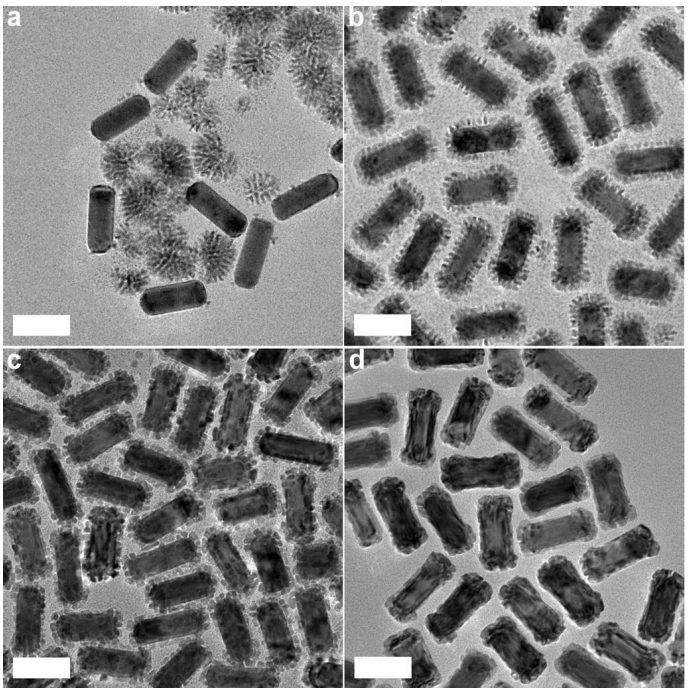

Figure S7. CPC concentration influence on production of Au@Pd SSs. (a-d) TEM images of products prepared with using (a) 1 mM, (b) 10 mM, (c) 50 mM and (d) 100 mM of CPC as the structure directing agent, under other synthesis conditions identical to standard procedure. Unlabeled scale bars are 50 nm.

As shown in Fig. S7b, appropriate CPC concentration (10 mM) is necessary for production of Au@Pd SSs with high quality. For instance, low concentration (1 mM) of CPC only gives rise to isolated Pd NPs (Fig. S7a), while too high concentration (50 or 100 mM) of CPC is favorable for generating rough Pd domains (Fig. S7c) or even thin Pd shells (Fig. S7d) on the surfaces of Au NRs.

Part S4. Supporting Information of SPR Properties of Au@Pd SSs

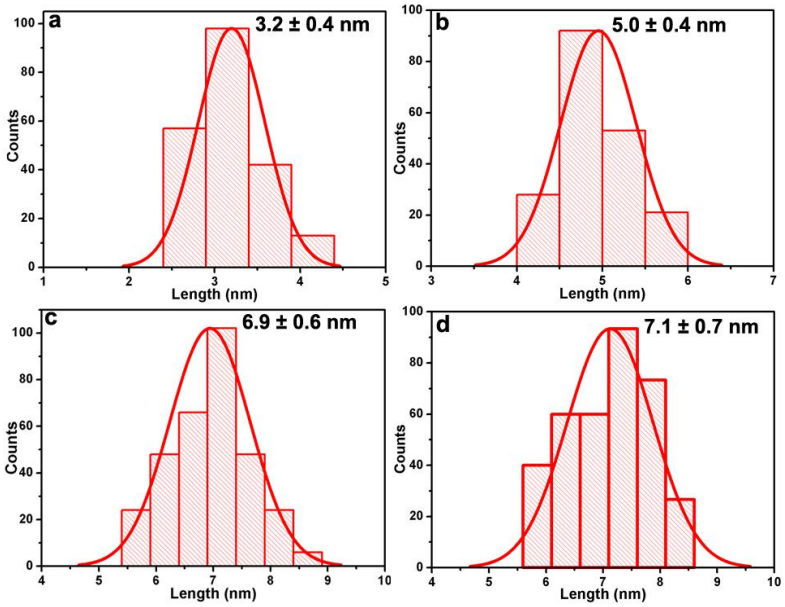

Figure S8. Statistic length of Pd nanorrays. (a-d) Statistic histograms of average length of Pd nanorrays in Au@Pd SSs with increasing Pd precursors in Fig. 3 b-e, respectively.

As shown in Fig. S8a-c, the average length of Pd nanoarrays in the resultant Au@Pd SSs could be controlled from 3.2 ± 0.4 to 5.0 ± 0.4 and 6.9 ± 0.6 nm through increasing the amount of Pd precursors. The fact that no obvious change is obtained with further addition of Pd precursors demonstrates complete formation of intact Pd nanoarrays onto the surfaces of Au NRs.

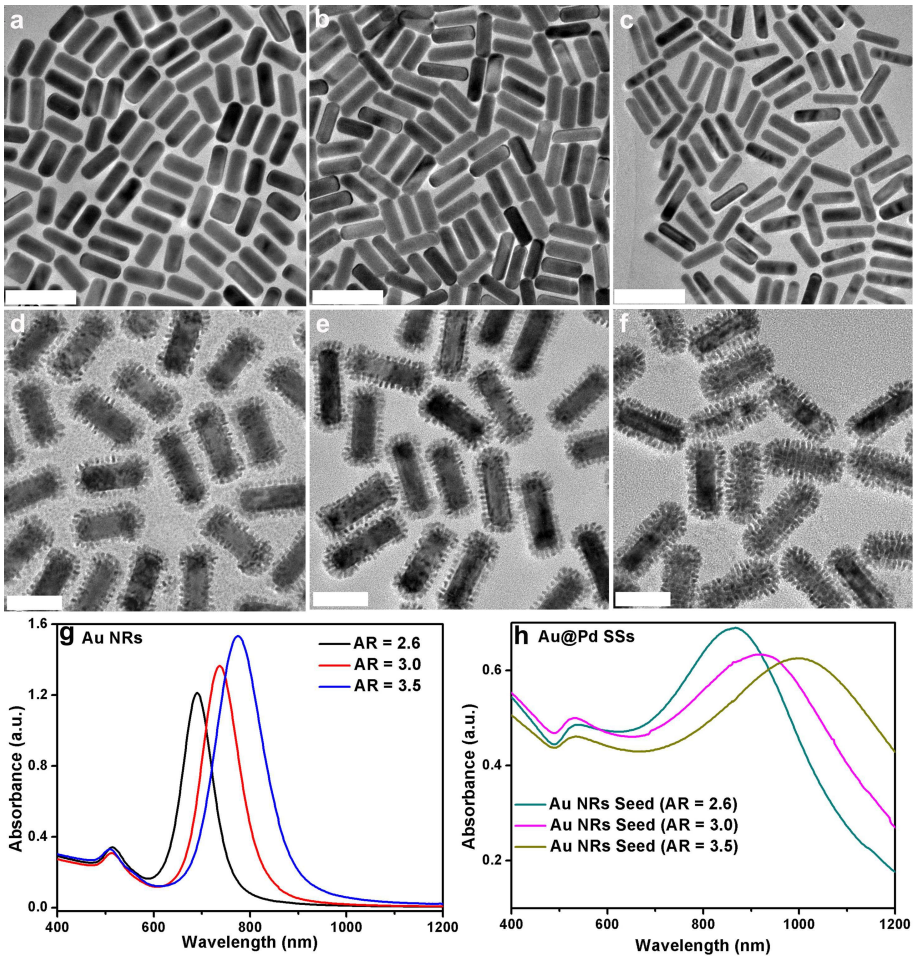

Figure S9. Tuning SPR band of Au@Pd SSs via varying AR of Au NRs seeds. (a-c) TEM images of Au NRs with aspect ratio (AR) of 2.6, 3.0 and 3.5, respectively. (d-f) TEM images of Au@Pd SSs obtained with the corresponding Au NR seeds, respectively. (g,h) Vis-NIR spectra of bare Au NRs and corresponding Au@Pd SSs, respectively. Unlabeled scale bars in (a-c) and (d-f) are 100 nm and 50 nm, respectively.

The surface plasmon resonance (SPR) band of Au@Pd SSs could be tuned to NIR region by varying the AR of Au NR seeds. And their strong light absorption in both visible (transverse SPR, TSPR) and NIR region (longitudinal SPR, LSPR) enables Au@Pd SSs efficient utilization of whole solar energy.

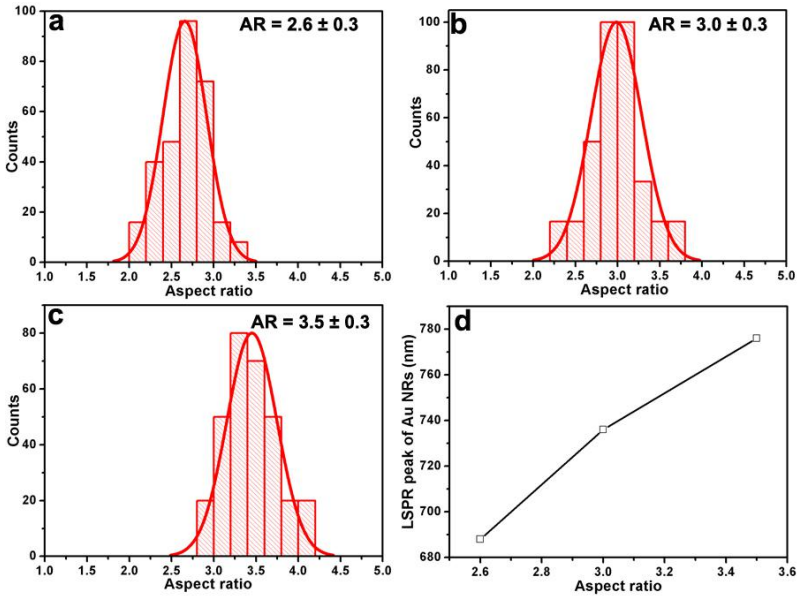

Figure S10. Statistic AR of Au NRs. (a-c) Statistic histograms of average AR of Au NRs in Fig. S9a-c, respectively. (d) Linear relationship between LSPR peak positions against AR of Au NRs.

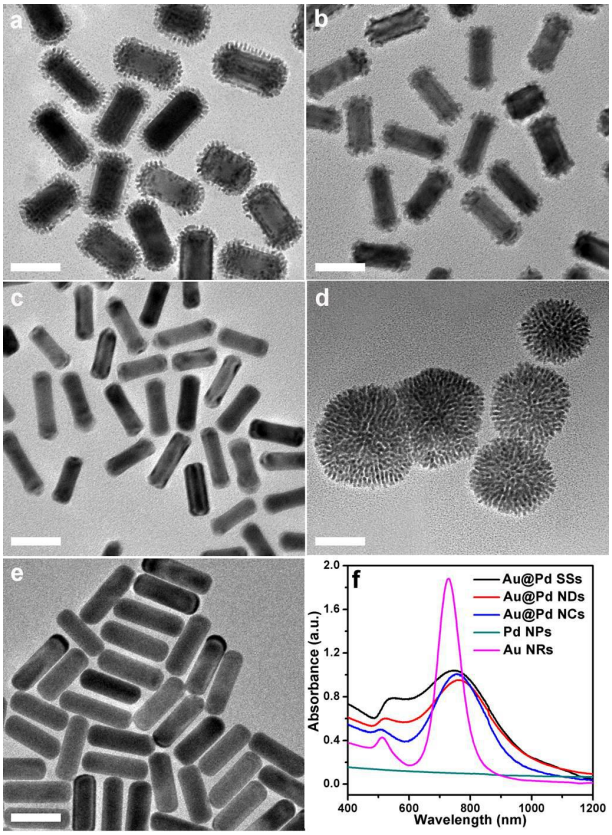

Figure S11. Characterization of contrast nanostructures. (a-e) TEM images of (a) Au@Pd SSs, (b) Au@Pd NDs, (c) Au@Pd NCs, (d) porous Pd NPs, and (e) bare Au NRs. (f) Corresponding Vis-NIR absorption spectra. Unlabeled scale bars are 50 nm.

As shown in Fig. S11, the LSPR band of the contrast samples (except for porous Pd NPs) is adjusted to be close to that of Au@Pd SSs for comparison.

Table S1. ICP-MS result of the tested catalysts.

Catalyst	Au amount (μg)	Pd amount (μg)
Au NRs	49.4	-
Pd NPs	-	9.6
Au/Pd Mixture	49.4	9.6
Au@Pd SSs	49.4	9.6
Au@Pd NDs	50.6	11.6
Au@Pd CSs	48.2	11.4

As data shown in Tab. S1, both Au or/and Pd amount in all the contrast samples is comparable with that of Au@Pd SSs, thus ensuring that the activity comparison of all the catalysts is reliable.

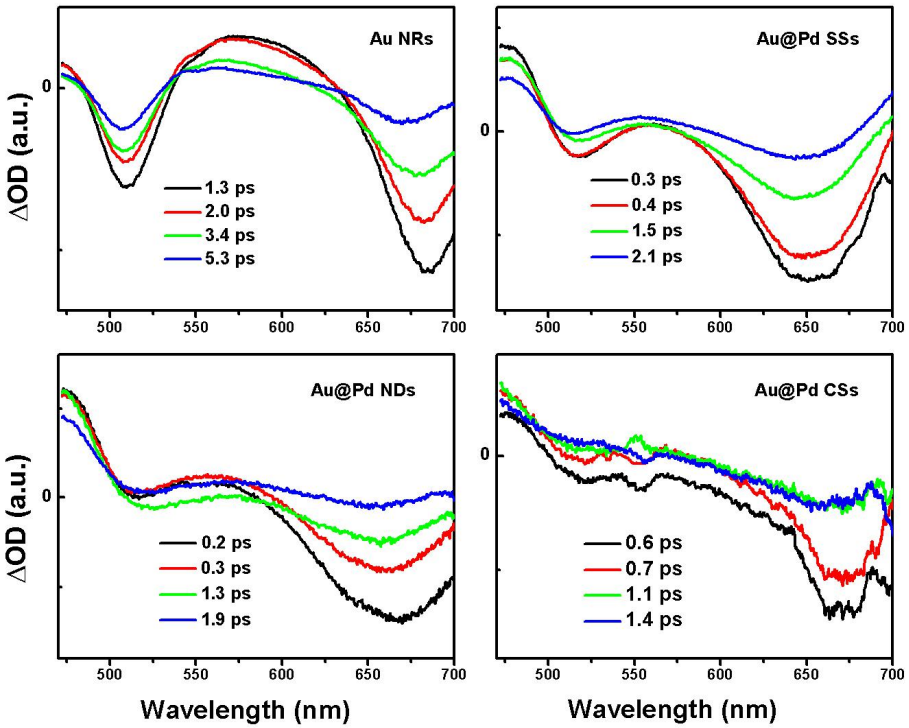

Figure S12. Transient absorption spectra of diverse nanostructures at representative delay time.

The obtained negative Δ OD signals around LSPR bands stand for the transient broadening of LSPR bands due to production of hot electrons, which decreases in magnitude with time.

Part S5. Supporting Information of Plasmon-Enhanced Catalysis Test

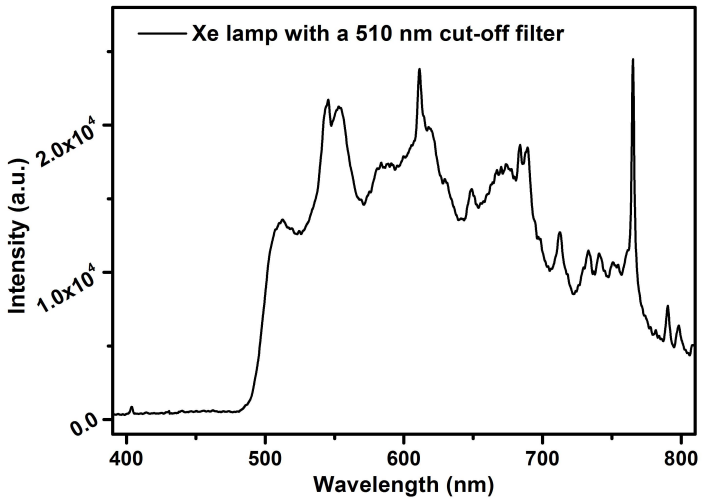

Figure S13. The output spectrum of the Xe lamp installed with a 510 nm long-pass filter used in our experiments.

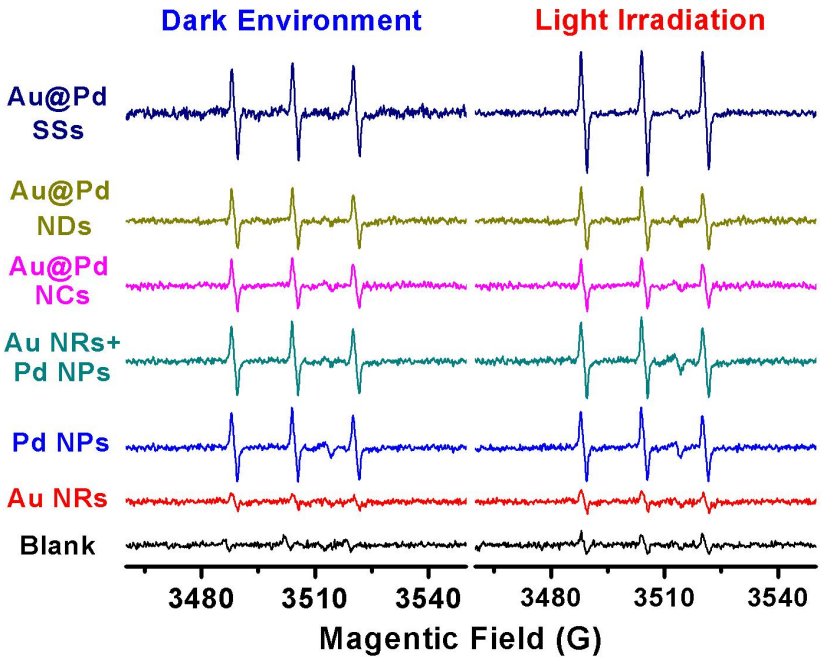

Figure S14. ESR spectrum of tested nanostructures. Each aqueous samples containing 0.09 M TEMP and tested nanostructures under both dark and light irradiation condition.

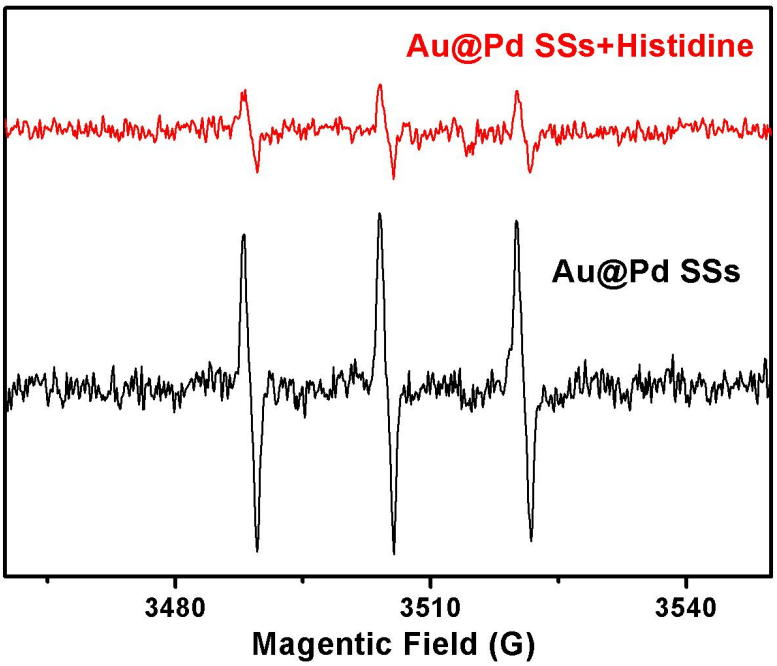

Figure S15. ESR spectra of TEMPO quenched by histidine. Sample solution containing TEMP and Au@Pd SSs with (red curve) and without (black curve) adding histidine as $^1O_2$ quencher.

Fig. S15 shows that the ESR signal of the produced TEMPO adduct is obviously quenched by adding histidine, further disclosing formation of $^1O_2$ specie in the solution.

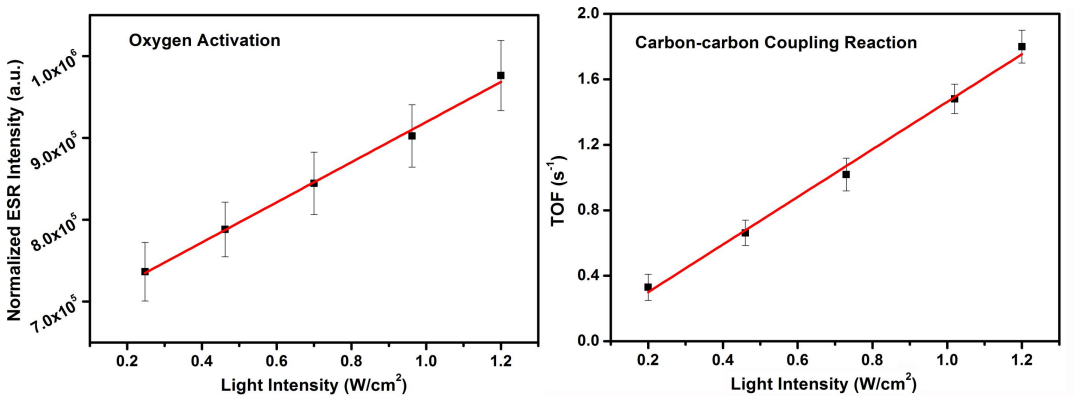

Figure S16. The light intensity-dependent reaction rates of Au@Pd SSs in oxygen activation and carbon-carbon coupling reaction, corresponding data were averaged based on three parallel tests.

The obtained good linear relationships between the reaction rate and light intensity in our two cases confirm that the photon flux is directly absorbed for driving the catalytic reaction and that photothermal effect is negligible in our systems.

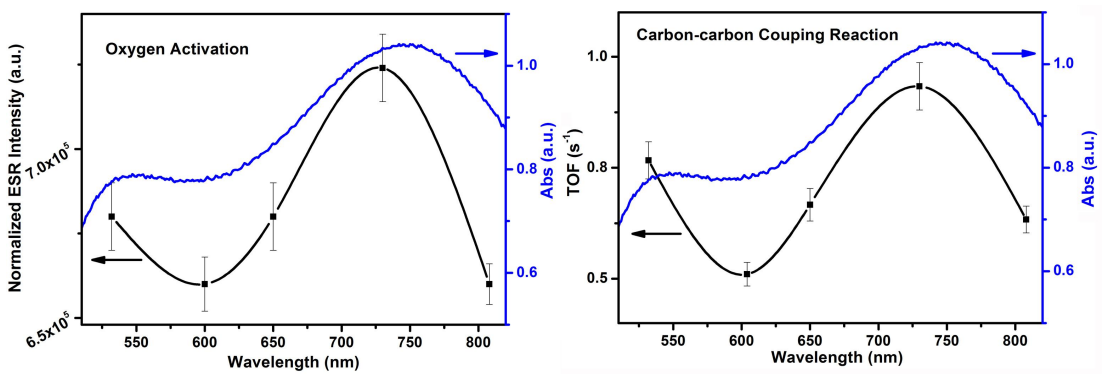

Figure S17. Comparison of the absorption spectrum and the wavelength-dependent performance of Au@Pd SSs in oxygen activation and carbon-carbon coupling reaction, corresponding data were averaged based on three parallel tests. The light intensity at each wavelength is kept at 0.3 W/cm^2.

As results shown in Fig. S17, good consistency between the wavelength-dependent performance and corresponding absorption spectrum indicates that the SPR absorption of catalyst indeed affects the two catalytic reactions.

Part S6. Theory Calculation of Photothermal Effect of Au@Pd SSs

Based on energy conversion principle, the temperature distribution throughout the particle and its surroundings can be written by the time-dependent equation (1):

$$\rho(r)c(r)\partial_t T(r,t) = k(r)\nabla^2 T(r,t) + p(r,t) \quad (1)$$

Where $\rho(r)$, $c(r)$ and $k(r)$ stand for the mass density, specific heat and thermal conductivity, respectively. $T(r,t)$ is the temperature as a function of coordinate and time, while $p(r,t)$ is the importing power intensity and herein represents the light power absorbed by noble metal nanoparticles (NPs).

Under continuous light power, the above equation at steady state could be expressed to:

$$\nabla \cdot [k(r)\nabla T(r)] = -p(r) \quad (2)$$

For simplification, gold nanosphere with radius of R dispersed in water is considered as a model firstly. Considering the much higher thermal conductivity of Au than that of water (318.0 W m^{-1} K^{-1} *vs* 0.6 W m^{-1} K^{-1})[S3], the temperature distributed in Au NP may be treated equally and the total absorption power is:

$$\int p(r)dr = I\sigma_{\text{abs}} \quad (3)$$

For sphere symmetry Au NP, equation (2) is derived to:

$$4\pi r^2 k_{\text{w}} \nabla T(r) = -I\sigma_{abs} \quad (r > R) \quad (4)$$

And we obtain:

$$\Delta T_{\text{NP}} = \frac{I\sigma_{\text{abs}}}{4\pi R k_{\text{w}}} \quad (5)$$

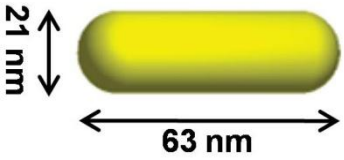

Au NR model in our calculation

For nonspherical Au NR, the above equation should be revised by adding a dimensionless thermal-capacitance coefficient $\beta(\text{AR})$, which is a function of aspect

ratio (AR) of Au NR[S4]: $\beta(\mathrm{AR}) = 1 + 0.96587 \ln^2(\mathrm{AR})$ and affords following equation:

$$\Delta T_{\mathrm{NP}} = \frac{I\sigma_{\mathrm{abs}}}{4\pi R_{\mathrm{eq}}\beta(\mathrm{AR})k_{\mathrm{w}}} \quad (6)$$

Where σ_{abs}, I and k_{w} are the absorption cross section of Au NR at LSPR wavelength (6820 nm^2), power intensity of incoming light (0.7 W cm^{-2}) and conductivity of water (0.6 W m^{-1} K^{-1}), respectively. R_{eq} is the equal radius (16.7 nm) of Au NR having same volume of a nanosphere, and $\beta(\mathrm{AR}=3.0)$ is calculated to be 2.16 in our model. Altogether, the ΔT_{NP} is calculated to be ~1.7×10^{-4} K.

It should be stressed that in our calculation, the Au@Pd SSs are replaced with Au NRs as the model and the incoming light power (0.7 W cm^{-2}) is treated as mono-wavelength light centered at the LSPR of Au NR for simplifying. Nevertheless, both treatments would slightly overestimate the ΔT_{NP} value, thus not influencing our analysis and discussion.

Part S7. Supplementary References

(1) Ye, X.; Gao, Y.; Chen, J.; Reifsnyder, D. C.; Zheng, C.; Murray, C. B., *Nano Lett.* **2013,** *13*, 2163.

(2) Huang, X.; Li, Y.; Chen, Y.; Zhou, E.; Xu, Y.; Zhou, H.; Duan, X.; Huang, Y., *Angew. Chem. Int. Ed* **2013,** *52*, 2520.

(3) Benenson, W.; Harris, J. W.; Stöcker, H.; Lutz, H., *Handbook of physics*. Springer-Verlag, New York: 2000.

(4) Baffou, G.; Quidant, R.; Abajo, F. J. G. D., *ACS Nano* **2010,** *4*, 709.